146 Chem. Rev. **2010,** *110,* 146–177

Block Copolymer Based Nanostructures: Materials, Processes, and Applications to Electronics

Ho-Cheol Kim,* Sang-Min Park, and William D. Hinsberg

IBM Research Division, Almaden Research Center, 650 Harry Road, San Jose, California 95120

Received April 21, 2009

Contents

1. Introduction

Block copolymers have attracted increasing interest due to their ability to self-organize at nanometer scales.[1−18] When the strength of the repulsive interaction between blocks is sufficiently large, the molecular architecture of a block copolymer, which consists of two or more chemically distinct homopolymers tethered to each other, leads to microphase separation of dissimilar polymer chains into periodic domains whether in the melt, solid state, or solution. Typical dimensions of these microdomains range from 5 to 50 nm, a span that encompasses those required by the semiconductor industry for the fabrication of future integrated circuits.

The rate of advancement of modern semiconductor devices is governed by the ability to create scaled high-resolution patterns on substrates of electronic materials. Today, conventional UV photolithography can produce structures of arbitrary shape at dimensions below 40 nm with remarkable speed and efficiency, the cumulative result of decades of engineering refinements.[19] It is widely recognized that further improvements will be accompanied by rapid increasing cost and difficulty, and given current understanding it is not anticipated that state-of-the-art 193 nm immersion lithography can be extended beyond the 22 nm node.[20] Prospective replacement technologies such as extreme UV lithography and nanoimprint lithography still face significant technical hurdles,[21,22] so it is difficult to predict their readiness for future device generations. Consideration of these issues has heightened an already growing interest in the use of self-assembly of materials as a means for patterning solid surfaces.[5,6,9,10,15,23] Self-assembly in principle can provide well-organized structures with atomic or molecular level precision (though such precise control over the assembly process and the final structure is not yet routine). In an ultimate application of self-assembly, nanoscale device components (e.g., semiconductor nanoparticles) might be directly deposited on a substrate in a self-organized fashion to form a functioning circuit.[24] Most applications of block copolymers in electronics are more modest and seek to harness their self-assembling properties so they may substitute for the polymeric photoresist films[25] used in current practice. This approach offers a nearer term opportunity to exploit the benefits of self-assembly (nanoscopic structures of dimensions far smaller than those offered by optical lithography by a simple process and at low cost) in an incremental, evolutionary way. With this goal, tremendous effort has been devoted over more than a decade to explore the practical applications of block-copolymer-based nanostructures.

While the spatial scale and process simplicity are attractive, much work remains before block-copolymer self-assembly will find broad practical use in electronics application.[26] In general, the materials must satisfy numerous other functional requirements (for example, compatibility with other materials or resistance to erosion in a plasma environment) as dictated

---

* To whom correspondence should be addressed. Phone: 408-927-3725. Fax: 408-927-3310. E-mail: hckim@us.ibm.com.

10.1021/cr900159v

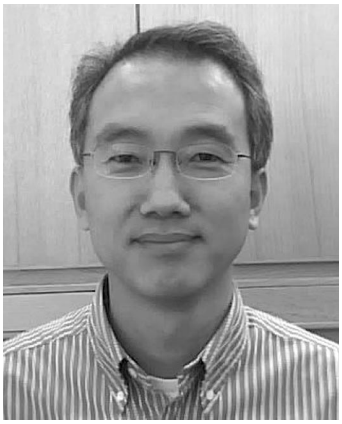

Ho-Cheol Kim received his B.S., M.S., and Ph. D. degrees from Seoul National University in Korea. Following his postdoctoral research in the Polymer Science and Engineering Department at the University of Massachusetts at Amherst, he joined the IBM Almaden Research Center in 2001. Currently he is a Research Staff Member in the Advanced Organic Materials Group. His research interests are nanostructures of self-assembled functional hybrid materials, especially for surface nanopatterning, nanostructured solar cells, and electrical energy storage applications. He has received the IBM Research Division Award in 2005 for advances in creation of controlled nanostructures. He has authored or coauthored over 90 research publications, mentored over 35 undergraduate and graduate students, and holds 13 issued U.S. patents.

Sang-Min Park received his B.S. degree in Polymer Science and Engineering from Chungnam National University (Korea) in 2000 and M.S. degree in Material Science and Engineering from POSTECH (Korea) in 2002. He did graduate work in Material Science at the University of Wisconsin—Madison under the supervision of Professor Paul F. Nealey and obtained his Ph.D. degree in 2007. He then joined the IBM-Almaden Research Center as a Postdoctoral researcher. His research interests include sublithographic nanopatterning of solid surfaces using thin films of block copolymers and block-copolymer-based nanostructures for device fabrications.

William Hinsberg received his doctorate degree in Chemistry at the California Institute of Technology and carried out postdoctoral work at Stanford University. In 1982, he joined IBM's General Products Division, working in thin film process chemistry for magnetic recording devices. He moved to IBM's Research Division in 1983 to study the chemistry of new photoresist materials. He currently is manager of the Lithography Materials group at the IBM Almaden Research Center. Four photoresists developed by Dr. Hinsberg and co-workers have been used by IBM for the commercial manufacture of microelectronic devices. He has received a number of awards from IBM for his technical work, including his selection as a Top Inventor of IBM and a Corporate Award for the development of stochastic chemical kinetics simulation methods. He has published more than 120 scientific papers and is inventor on 30 issued patents. He is a recipient of the 1998 Leo J. Friend Award sponsored by the Industrial and Engineering Chemistry Section of the American Chemical Society. He also received the 1998/1999 Award for Chemical Engineering Excellence from the Northern California Section of the American Institute of Chemical Engineers.

by the specific application. Moreover, the highly periodic nature of the microdomains places significant restrictions on how block-copolymer-based surface patterning can be implemented, and this must be considered in process and device design. Finally, the development of optimal block-copolymer materials and of new assembly methods for controlling placement of microdomains on the surface in conjunction with traditional photolithography still stand as challenges.

In this review, we survey materials and methods for carrying out the controlled assembly of block copolymers in thin films for a variety of nanofabrication applications. It should be noted that this field is developing rapidly, and the research directions are diverse; thus, it is almost impossible to capture a comprehensive literature review in a single article. We strive to include as many literature citations as possible within the topics selected for discussion in this review. We organize this review as follows: a brief introduction to block copolymers, their hybrids, and self-assembly behavior is presented in section 2. In section 3, we discuss methods for assembly of block copolymers in thin films. This includes a description of the basic principles that govern ordering of microdomains, various processing methods to achieve ordering, and an in-depth discussion of techniques for controlling placement of microdomains, often referred to as directed self-assembly. In section 4, previous efforts on applications of block-copolymer-based nanostructures are reviewed, limiting our discussion to the fabrication of nanostructures for electronics applications. In section 5, we summarize the limitations of block-copolymer-based nanostructures. Section 6 enumerates the functional attributes these materials must possess to find broad practical application, and finally, we provide an outlook in section 7.

2. Materials

2.1. Diblock Copolymers

Block copolymers are a specific class of copolymer (polymers comprising more than one chemically distinct monomer) where the different monomers are not distributed within the polymer chain in random or alternating fashion but instead are grouped in discrete homogeneous sections (or blocks) of the chain.[27] Conceptually a block copolymer can be thought of as two or more distinct homopolymers linked end to end through covalent bonds. The number of distinct homopolymer homogeneous sections determines the molecular architecture of block copolymer; diblock, triblock, and higher multiblock copolymers are possible.[16] Diblock copolymers which contain two distinct

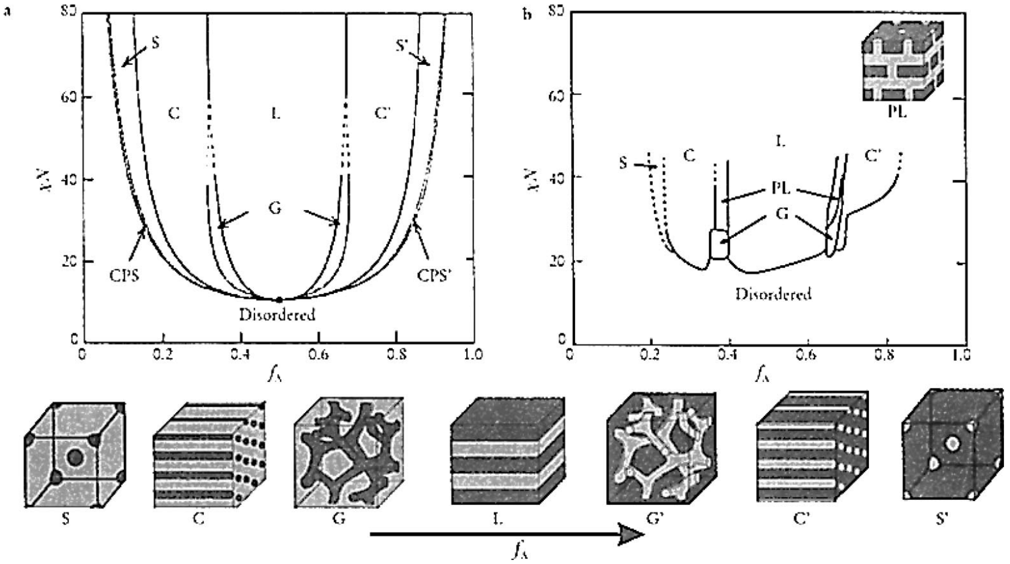

Figure 1. Phase diagram for linear AB diblock copolymers. (Left) Equilibrium morphologies predicted by self-consistent mean-field theory: spherical (S), cylindrical (C), gyroid (G), and lamellar (L). (Right) Experimental phase diagram of poly(styrene-*b*-isoprene) (PS-*b*-PI) diblock copolymers: perforated layers (PL). (Bottom) A representation of the equilibrium microdomain structures as f_A is increased for fixed χN. (Reprinted with permission from ref 16. Copyright 1999 American Institute of Physics.)

homopolymers are the simplest molecular architecture of block copolymers and have been studied most extensively for generating a variety of nanostructures. Just as most polymer mixtures will separate into different phases, the two blocks of a diblock copolymer tend to demix. The covalent bond linking the blocks, however, prevents the macroscopic phase separation observed in binary mixtures of the homopolymers and results in nanoscale structural organization of each block.

The phase behavior of diblock copolymers has been studied extensively from both experimental and theoretical perspectives.[28−33] For surveys of past work on the phase behavior of block copolymers, the reader is directed to the books and review articles cited in refs 16, 27, and 33. In short, the propensity for block copolymers to phase separate into periodic microdomains is determined by the strength of the repulsive interaction as characterized by the product χN, where χ is the Flory−Huggins interaction parameter[34,35] and N is the number of monomers in the diblock copolymer. Microphase separation can occur when this value exceeds the critical value for the order−disorder transition. At equilibrium, this microphase separation is established by a delicate energy balance between the stretching energy for the polymer chains and the energy of interactions at the interface between A and B microdomains. In diblock copolymers, the morphology of the microdomains ranges from spheres to cylinders to lamellae depending on the volume fraction of one block. Figure 1 presents a

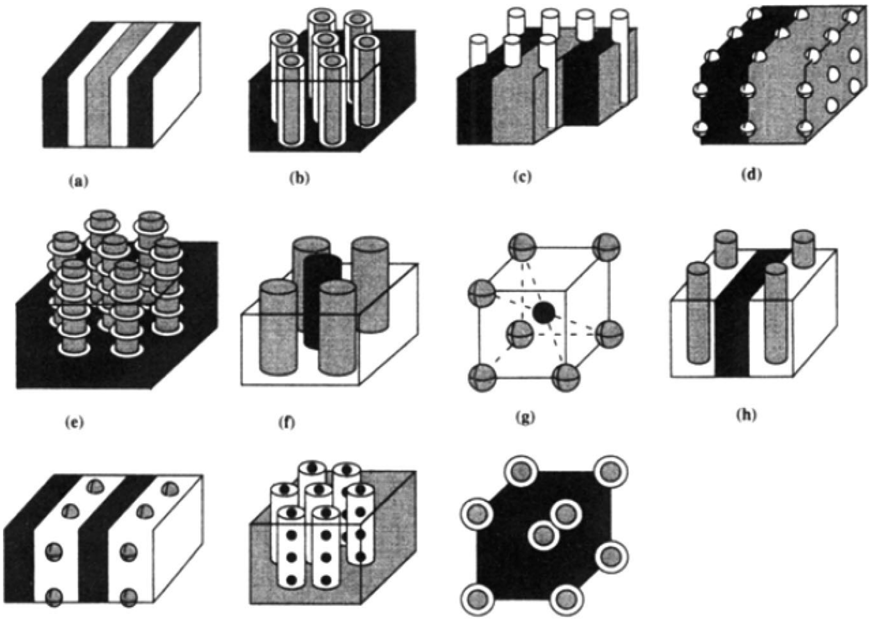

Figure 2. Schematic representation of the phases of ABC triblock copolymers. Dark, A; white, B; gray, C. (a) Lamellar phase; (b) coaxial cylinder phases; (c) lamella−cylinder phase; (d) lamella−sphere phase; (e) cylinder−ring phase; (f) cylindrical domains in a square lattice structure; (g) spherical domains in the CsCl-type structure; (h) lamella−cylinder-II; (i) lamella−sphere-II; (j) cylinder−sphere; (k) concentric spherical domain in the bcc structure. (Reprinted with permission from ref 42. Copyright 1995 American Chemical Society.)

theoretical and an experimental phase diagram of a model diblock copolymer, poly(styrene-*b*-isoprene) (PS-*b*-PI).[16] The phase diagram shows the dependence of morphology on the volume fractions (f_A, f_B) of the two blocks. An order−disorder transition will occur when χN falls below a critical value. This occurs, for example, at very low molecular weight (where N is small) or high temperature (since $\chi \approx a + b/T$) for a given molecular weight. In Figure 1 the theoretical critical value is 10.4 for the case of a symmetric copolymer.

The size of microdomains scales with the copolymer molecular weight. For symmetric diblock copolymers, which have the simplest lamellar morphology, the size of microdomains is often denoted as the natural period L_0 that corresponds to the length of two copolymer molecules in the ordered state. The scaling law that describes how the scale of lamellar microdomains depends on the degree of segregation (i.e., the strength of the repulsive interaction between two blocks) has been studied in depth. Although different theoretical approaches have been pursued by several groups,[29,32,36−38] all theoretical predictions describe the molecular weight dependence of L_0 as the power law $L_0 \propto N^{\alpha}$, where the exponent α varies with the degree of phase separation. In the strong segregation limit (SSL) where χN is large, mean-field theory suggests that L_0 scales with $N^{2/3}$. This 2/3 power law has been demonstrated experimentally by many research groups including Hashimoto and coworkers.[32] In the weak segregation limit (WSL) where χN is reduced to a value near the order−disorder transition point, L_0 scales as $N^{1/2}$. The region between SSL and WSL is the so-called intermediate segregation region (ISR) where the value of α varies theoretically from 0.72 to 1.017 and experimentally from 0.8 to 0.83.[39−41] Recent work of Sivaniah and co-workers on pure and blended symmetric poly(styrene-*b*-methyl methacrylate) (PS-*b*-PMMA) thin films showed an exponent of 0.85 for block copolymers in the ranges of $40 < \chi N < 100$, which corresponds to the ISR.[36]

2.2. Triblock Copolymers

Triblock copolymers consist of three distinct homopolymers, A, B, and C, that are covalently bonded together. The microphase separation of ABC triblock copolymers is much more complicated than that of diblock copolymers. While the phase behavior of a diblock copolymer is governed by three factors (N, f, χ) additional distinct new parameters determine the phase behavior of triblock copolymers. In the triblock case there are three interaction parameters (between A−B, B−C, and C−A) and the morphology depends not only on the temperature, molecular weight, and fraction of each block but also on the sequence of blocks in the chain, relative magnitude of the interaction parameters, and overall composition. Thus, a richer and more complex morphology of microdomains is anticipated with triblock copolymers. Zheng and Wang reported a theoretical calculation of the morphological phase diagram for ABC triblock copolymers in the SSL.[42] A variety of microdomain structures considered in their report are schematically presented in Figure 2.

Experimental observation of the new ordered structures in ABC triblock copolymers has confirmed the complexity of microdomain morphology. In a series of papers, Stadler and co-workers reported on the morphological investigation of ABC triblock copolymers using transmission electron microscopy (TEM).[43−47] They used triblock copolymers based on poly(styrene-*b*-butadiene-*b*-methyl methacrylate) (PS-*b*-PB-*b*-PMMA) and their hydrogenated analogues poly(styrene-*b*-(ethylene-co-butylene)-*b*-methyl methacrylate) (PS-*b*-PEB-*b*-PMMA, SEBM)) and found the morphology is governed by the relatively weak incompatibility of the end blocks PS and PMMA rather than the strong incompatibility of the polybutadiene (PB) or poly(ethylene-*co*-butylene) (PEB, EB) midblock. As shown in Figures 3 and 4, remarkable microdomain morphologies have been produced by varying the fraction of the midblock while holding the outer blocks approximately constant. The left column of Figure 3 shows TEM images of an SEBM film wherein EB cylinders appear as spherical microdomains between PS and PMMA lamellae; the polymer composition in this instance is S:EB:M equal to 48:17:35 wt %, respectively. The right column of Figure 3 shows TEM images of an SEBM film where the EB fraction is much reduced (S:EB:M equal to 45:6:49 wt %, respectively). In this film the EB forms rings encircling PS cylinders that are dispersed in the PMMA matrix. Figure 4 shows the so-called "knitting patterns" formed in an SEBM film where the EB fraction is 27 wt %. It is noted that potential applications of these complex morphologies have not been extensively explored, although these unique ordered microdomains potentially provide rich structures for nanofabrication that are difficult to fashion by other methods.

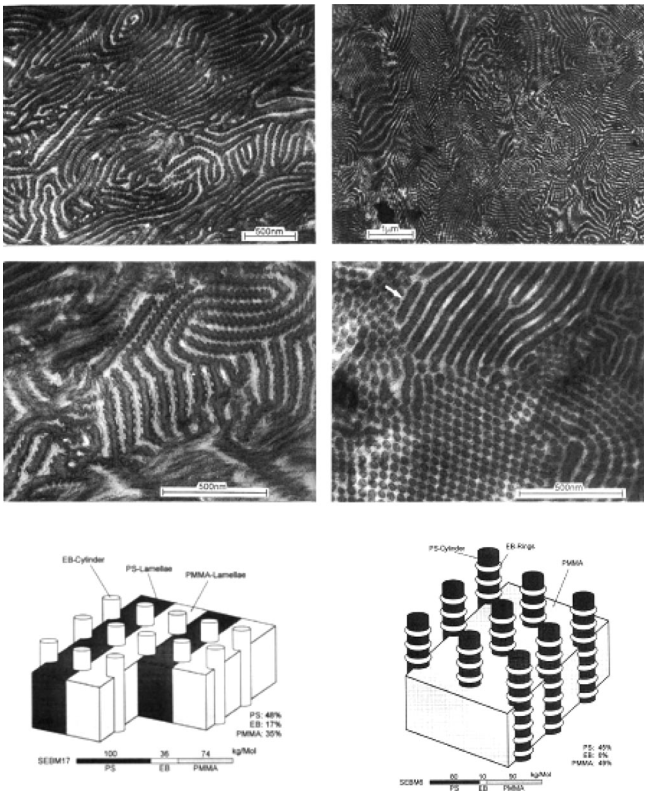

Figure 3. (Left) Morphology of the triblock-copolymer SEBM 17 at (top) moderate magnification and (middle) higher magnification: dark, PS lamellae; bright, PMMA lamellae. The cross sections of the EB cylinders appear as spherical microdomains between the PS and the PMMA lamellae. (Bottom) Schematic representation of the morphology of the triblock-copolymer SEBM17 with EB cylinders between the PS and PMMA lamellae. (Right) Morphology of the triblock-copolymer SEBM6 at (top) moderate magnification and (middle) higher magnification. The EB rings around the PS cylinders can be recognized as small spherical cross sections on the surface of the PS domains (see arrow). (Bottom) Schematic representation of the morphology of the triblock-copolymer SEBM6 with PS cylinders dispersed in a PMMA matrix and isolated small EB rings around the PS cylinders. (Reprinted with permission from ref 43. Copyright 1993 American Chemical Society.)

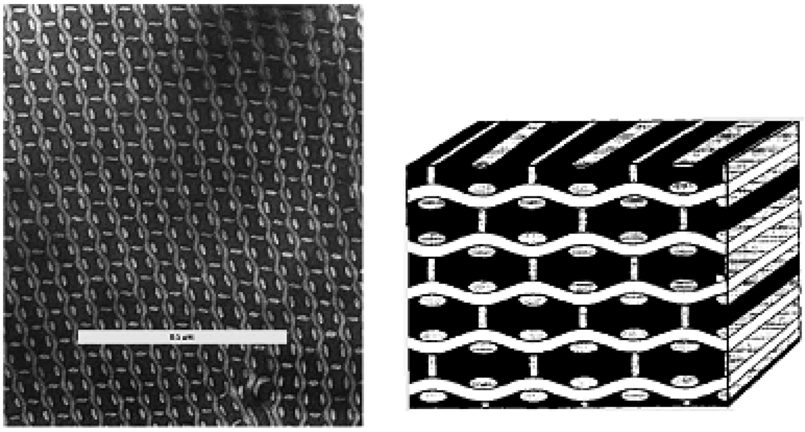

Figure 4. (Left) Bright-field transmission electron micrograph of copolymer SEBM27 stained with RuO_4 (scale bar, 0.5 μm). (Right) Three-dimensional model of “knitting pattern (kp)” morphology. (Reprinted with permission from ref 47. Copyright 1996 Wiley-VCH Verlag GmbH & Co. KGaA.)

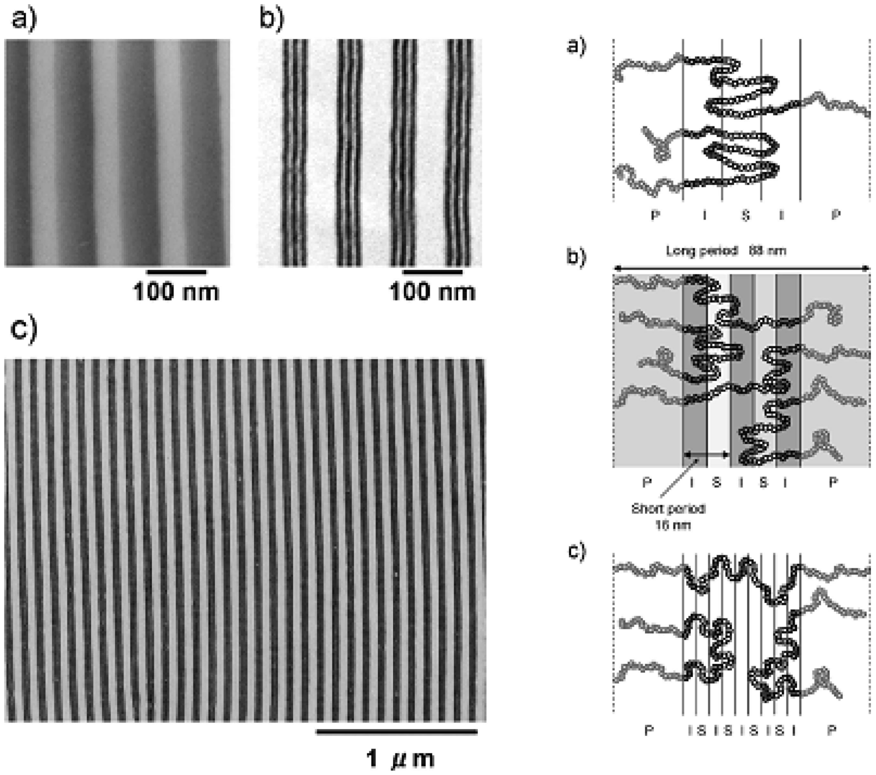

Figure 5. (Left) Bright field transmission electron micrographs of the PISISISISIP undecablock terpolymer. Sample specimens are ultrathin sections cut from a solvent-cast and annealed film. Ultrathin sections were stained with iodine for a and osmium tetroxide for b and c. (Right) Possible molecular conformations of the undecablock terpolymer in lamellar nanophase-separated (a) three-layered, (b) five-layered, and (c) nine-layered structures. (Reprinted with permission from ref 53. Copyright 2006 American Physical Society.)

2.3. Multiblock Copolymers and Supramolecular Polymers

An essentially limitless variety of block polymer architectures extends beyond the AB diblock and ABC triblock systems. The phase behaviors of linear block copolymers with more complex molecular architectures have been studied, where systems such as $(AB)_n$ multiblock copolymers,[48] pentablock copolymers of the ABABA type,[49] and heptablock copolymers of ABABABA type[50] have been examined. An interesting study of the hierarchical microdomain structure of a multiblock copolymer was recently reported by Matsushita and co-workers as shown in Figure 5.[51−54] They prepared a undecablock copolymer which incorporates two long poly(2-vinylpyridine) (P2VP, P) blocks on each end and five short polyisoprene (PI, I) and four short polystyrene (PS, S) blocks at the center. An annealed film of this P-(I-S)$_4$-I-P material exhibits a hierarchical lamellar structure with two crystallographic periods. A theoretical investigation has predicted the number k of internal I and S layers for self-assembled P-(I-S)$_m$-I-P multiblock copolymers as a function of m.[52] The model prediction shows $k = 3, 5, 5, 7, 7, 9, ...$ for $m = 2, 3, 4, 5, 6, 7, ...$ The predicted value of $k = 5$ for the case where $m = 4$ is in good agreement with experimental observation.

Pursuing an alternative approach, self-assembly with multiple length scales has been demonstrated using polymeric supramolecular assembly. Ikkala and co-workers reported the formation of supramolecular nanostructures with several length scales using poly(styrene-*b*-4-vinylpyridine) (PS-*b*-P4VP) where the poly(4-vinylpyridine) (P4VP) block is

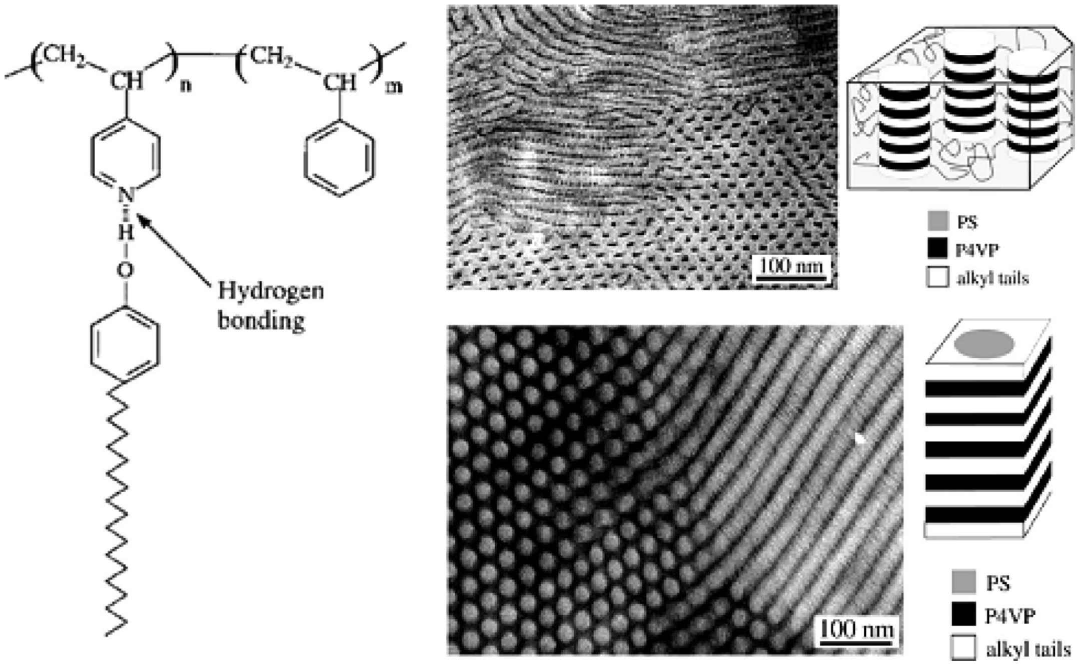

Figure 6. (Left) Scheme for supramolecular assembly of PS-*b*-P4VP and NDP. (Right) (top) TEM micrograph and schematics of lamellar-within-cylindrical structure of PS-*b*-P4VP $(NDP)_{1.0}$ with $f_{comb} = 0.27$; (bottom) TEM micrograph and schematics of cylindrical-within-lamellar structure of PS-*b*-P4VP $(NDP)_{1.0}$ with $f_{comb} = 0.65$. (Reprinted with permission from ref 55. Copyright 1999 Wiley-VCH Verlag GmbH & Co. KGaA.)

hydrogen bonded to an oligomeric amphiphile such as nonadecylphenol (NDP) (scheme in Figure 6).[55−59] This approach provides a variety of novel morphologies: lamellar-within-lamellar, lamellar-within-cylindrical, cylindrical-within-lamellar, spherical-with-lamellar, and lamellar-within-spherical structures can be formed depending on the effective weight fraction (f_{comb}) of the NDP-bonded P4VP block. Switching of phase morphology, which induces concurrent changes in functional properties, has been demonstrated by the same group. As shown in Figure 7, a mixture of P4VP with methanesulfonic acid (MSA) (which stoichiometrically protonates the P4VP) and pentadecylphenol (PDP) forms a microstructure with two different length scales. This microstructure changes with temperature and can be used to introduce temperature-dependent transitions in electrical conductivity.[56]

2.4. Block Copolymer Containing Hybrids

Since the pioneering work of Kresge et al.[60] to create ordered mesoporous silica, numerous extensions of that work using low or high molecular weight surfactants or amphiphilic block copolymers have been described.[61−66] The prevalent route to form mesoporous silica using amphiphilic block copolymers or surfactants is through sol−gel chemistry. Wiesner and co-workers reported the remarkably well-controlled formation of nanostructures of organically modified ceramic materials.[61] An amphiphilic poly(isoprene-*b*-ethylene oxide) (PI-*b*-PEO) block copolymer was used as a structure-directing agent during the sol−gel synthesis of an organically modified aluminosilicate network based on 3-(glycidyloxypropyl)trimethoxysilane (GLYMO) and aluminum *sec*-butoxide, $Al(O\text{-}s\text{-}Bu)_3$. As schematically shown in Figure 8, the aluminosilicate produced by reaction of GLYMO and $Al(O\text{-}s\text{-}Bu)_3$ preferentially swells the hydrophilic poly(ethylene oxide) (PEO) block of PI-*b*-PEO to form a nanostructured organic−inorganic

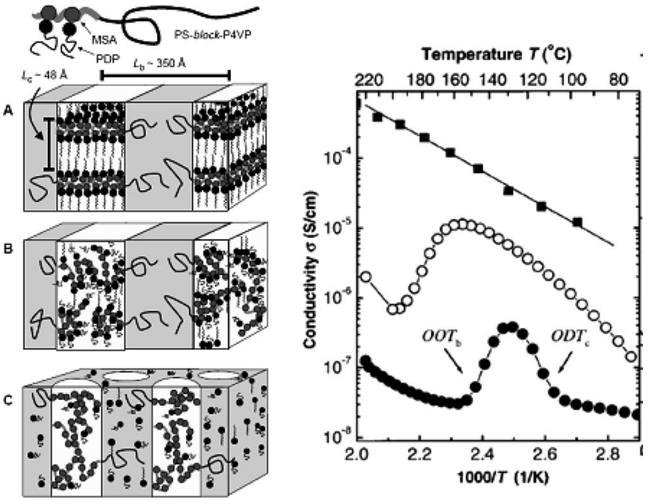

Figure 7. (Left) Schematic illustration of the self-organized structures of PS-*b*-$P4VP(MSA)_{1.0}(PDP)_{1.0}$. The local structures are indicated; macroscopically, the samples are isotropic. (A) Alternating PS layers and layers consisting of alternating one-dimensional slabs of $P4VP(MSA)_{1.0}$ and PDP for $T < T_{ODT}$. (B) Alternating two-dimensional PS and disordered $P4VP(MSA)_{1.0}(PDP)_{1.0}$ lamellae for $T_{ODTc} < T < T_{ODTb}$. (C) One-dimensional disordered $P4VP(MSA)_{1.0}(PDP)_x$ (with $x \ll 1$) cylinders within the three-dimensional PS-PDP medium for $T > T_{ODTb}$. (Right) Electrical conductivity (σ) during heating at 5 °C/min, on the basis of ac impedance measurements extrapolated to zero frequency. Similar data are observed during cooling. (■) $P4VP(MSA)_{1.0}$ showing the classical thermally activated conductivity. (○) $P4VP(MSA)_{1.0}(PDP)_{1.0}$ showing thermally activated behavior up to ∼160 °C, at which the first signals of imminent macrophase separation appear. A further increase in temperature results in a decrease in σ. The conductivity starts to increase again above ∼195 °C. (●) PS-*b*-$P4VP(MSA)_{1.0}(PDP)_{1.0}$, where an order−order transition (ODT_b) at the block-copolymer length scale has a distinct effect on the conductivity. The samples have not been oriented, and therefore, the results represent averages over all directions. The lines are drawn only to guide the eye. (Reprinted with permission from ref 56. Copyright 1998 American Association for the Advancement of Science.)

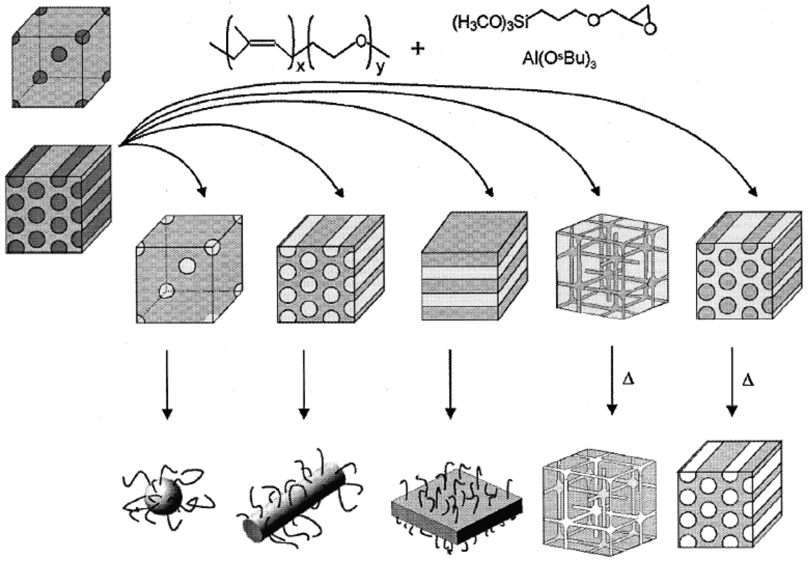

Figure 8. Schematic drawing for the preparation of nano-objects as well as mesoporous materials. (Reprinted with permission from ref 62. Copyright 2001 American Chemical Society.)

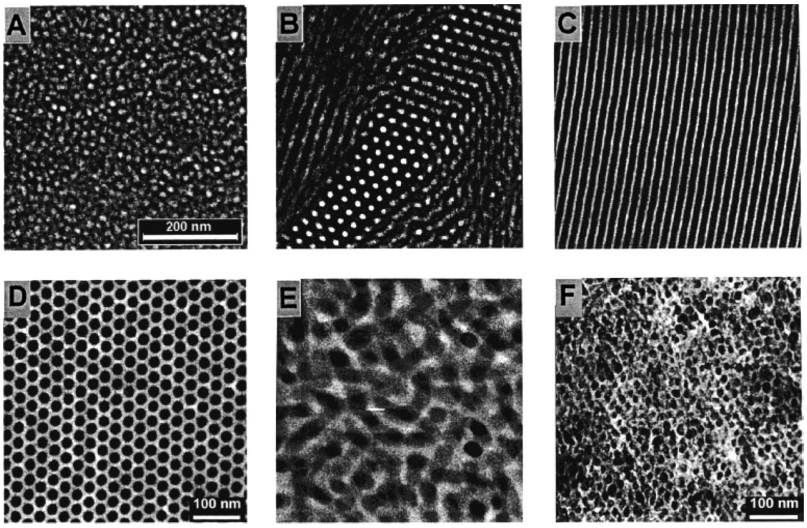

Figure 9. TEM micrographs of the GLYMO/Al(O-*s*-Bu)$_3$ hybrid materials (A) hex, (B) hex, (C) lam, (D) inv. hex, (E) wormlike micelles, and (F) inv. bcc shown all in the magnifications indicated by the bar in A if not otherwise indicated. Bulk samples having a PI matrix were stained with OsO$_4$ before and after ultrathin sectioning. Images of stained specimens were taken under bright field conditions. The PI and aluminosilicate are generally shown as the dark and bright phase, respectively. (Reprinted with permission from ref 62. Copyright 2001 American Chemical Society.)

hybrid.[62] The TEM micrographs shown in Figure 9 illustrate the variety of morphologies generated by this approach.

More recently, Kim and co-workers reported a simple path to prepare nanostructured organosilicate thin films using a poly(styrene-*b*-ethylene oxide) (PS-*b*-PEO) and a silsesquioxane-based oligomeric organosilicate (OS or PMS) precursor.[66−72] They used a commercially available OS that was first developed as an interlayer spin-on dielectric for microchips. As shown schematically in Figure 10, the OS is selectively miscible with PEO and the relative volume fraction of the PS and PEO+OS phases determines the morphology of coassembled nanostructures. Thermal treatment simultaneously cross links the OS and removes the PS-*b*-PEO, thereby providing OS nanostructures. This approach yields uniform films of nanostructured OS over large areas.

There is great interest in the potential for fabricating metallic nanoscale structures using a hybrid of block copolymers and nanoparticles or precursors. The preparation of metallic nanostructures by selectively decorating one of the microphase-separated domains with nanoparticles or metal ions has been demonstrated in numerous examples.[73−79] An alternative approach is based on the ordering of block copolymer/nanoparticle.[80,81] Figure 11 shows an example recently published by Chai and co-workers.[78] In this work, metal nanowires were formed by selectively incorporating metal ions into the P2VP microdomains of PS-*b*-P2VP block copolymer film, followed by plasma treatment. Though fabrication of electronic devices using these metal nanostructures has not yet been reported, potential pathways to apply this approach to device fabrication are clear.

Block-copolymer-mediated patterning of magnetic materials has been studied extensively. We will not address this body of work here and refer the reader to a recent in-depth review of the topic.[82]

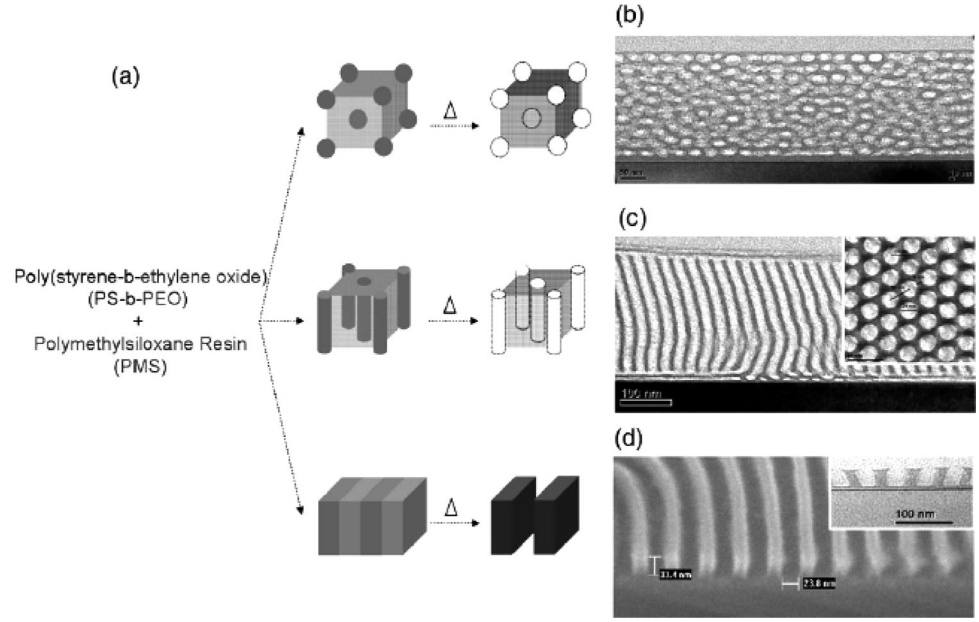

Figure 10. (a) Schematic presentation of the morphologies of the PS-*b*-PEO/PMS resin hybrid system. The volume fraction of the phases (i.e., PS, PEO + PMS resin) determines the morphology. The phase-separated structure can be fixed by thermal treatment at 150−180 °C. Porous nanostructures can be generated by removing the PS-*b*-PEO with high-temperature treatment (∼450 °C). (b−d) Electron micrographs of porous PMS resin with different morphologies. (b) Cross-sectional TEM image of thin PMS film containing spherical pores. (c) Cross-sectional and top-view (inset) TEM image of cylindrical pores. The inset shows hexagonally packed cylindrical pores. (d) Cross-sectional SEM and TEM (inset) images of lamellar PMS resin. (Reprinted with permission from ref 70. Copyright 2008 IOP Publishing Limited.)

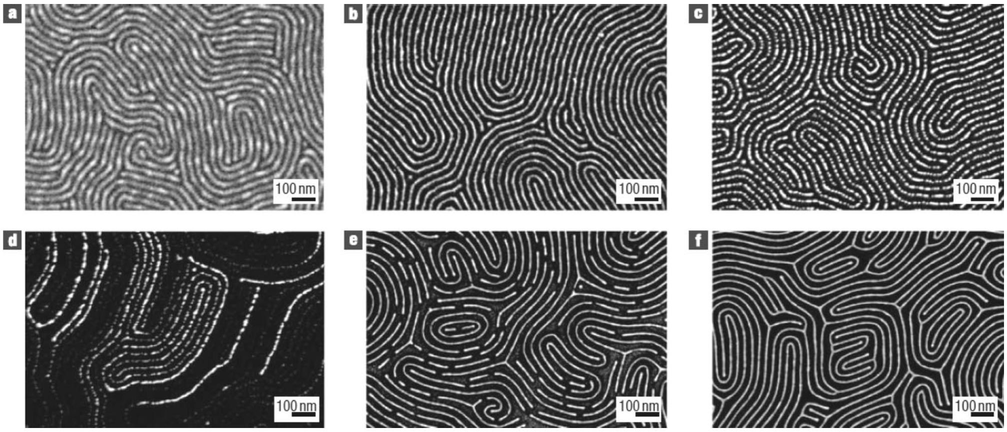

Figure 11. SEM images of gold, palladium, and platinum lines formed on a silicon substrate using a PS-*b*-P2VP copolymer template: (a) 0.1 mM $HAuCl_4$/0.9% HF(aq) for 10 min, (b) 10 mM $HAuCl_4$/0.9% HF(aq) for 10 min followed by 30 s oxygen plasma treatment, (c) 0.1 mM $HAuCl_4$/0.9% HF(aq) for 10 min followed by 30 s oxygen plasma treatment, (d) 0.1 M $HAuCl_4$(aq) for 24 h followed by 30 s oxygen plasma treatment, (e) 10 mM Na_2PdCl_4(aq)/0.9% HCl(aq) for 3 h followed by 30 s oxygen and 5 s argon plasma treatment, (f) 10 mM Na_2PtCl_4(aq)/0.9% HCl(aq) for 3 h followed by 30 s oxygen and 5 s argon plasma treatment. (Reprinted with permission from ref 78. Copyright 2007 Nature Publishing Group.)

3. Block Copolymer Ordering in Thin Films

In this section, we will review the ordering behavior of block copolymers and the block copolymer containing hybrid systems we have just described when they are prepared as thin films. Since the majority of studies have used diblock copolymers, we will focus our discussion on supported films of those materials. The behavior of both symmetric and asymmetric diblock copolymers will be examined.

3.1. General Process Steps

Although a variety of methods can be used for preparing thin films of block copolymers on substrates, the most popular method for film deposition is spin coating. In a typical spin-coating process, a solution of the polymer in a good solvent is dispensed onto a substrate, which is then spun at a speed of 1000−5000 rpm until the bulk of the solvent is evaporated from the film. The film thickness is determined by the concentration of the solution, the molecular weight of the polymer, and the spin speed.

The deposition is usually followed by an annealing step to facilitate or accelerate microdomain formation in the applied block-copolymer film. Annealing increases the mobility of the copolymer molecules, so the film can more rapidly reach its final structure. This is achieved by either a thermal or a solvent vapor treatment. In thermal annealing the sample is held at a temperature above the glass transition temperatures but below decomposition temperatures of the

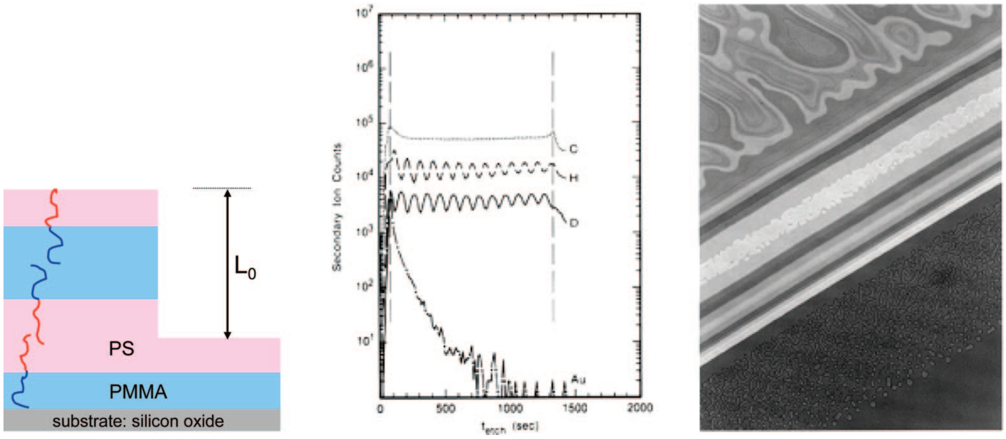

Figure 12. (Left) Schematic representation of ordered PS-*b*-PMMA thin film on a selective surface. (Middle) SIMS profile of a 5000 Å thick selectively deuterated dPS-*b*-PMMA copolymer sample annealed 72 h at 170 °C, shown as secondary ion counts versus etching time. The dashed vertical lines at lower and higher etching times mark the position of the air/copolymer and copolymer/silicon substrate interfaces, respectively. The C signal remains constant throughout the whole sample, while the H and D signals show pronounced oscillations. (Right) Interference colors observed at the edge of a dPS-*b*-PMMA copolymer sample annealed at 170 °C for 24 h. The full, long dimension of the micrograph shown is 280 μm. (Reprinted with permission from ref 38. Copyright 1989 American Chemical Society.)

blocks for a time sufficient to allow approach to the equilibrium morphology. It can be carried out under vacuum or in an inert gas environment.

In solvent vapor annealing the sample is held in a controlled atmosphere containing selected solvent vapors. Absorption of the vapor imparts greater mobility within the film. The efficacy depends on the selectivity of each block for the solvent, and a variety of solvents or mixtures of solvents can be used. Often, this solvent vapor treatment is used in conjunction with spin coating, i.e., the copolymer solution is applied to the substrate within a controlled solvent vapor environment. In this case, finely balanced interactions between solvent, copolymer, and the kinetics of solvent depletion govern the ordering of microdomains. This process has been used with success to control the orientation of cylindrical microdomains perpendicular to the surface under nonequilibrium conditions.[83]

For many practical uses, a three-dimensional relief image is the desired final nanostructural form, and with block-copolymer films this calls for a route to selectively remove one phase of the microdomain pattern. Similar to the pattern development step in lithography, UV flood irradiation followed by a solvent rinse has been used to remove PMMA microdomains from PS-*b*-PMMA patterns.[84,85] Though the etching selectivity between two organic blocks (e.g., PS and PMMA) is poor,[86] a dry etch process to remove PMMA domains from PS-*b*-PMMA using plasma etching has been optimized by some research groups.[87] With the PS-*b*-PEO+OS of Kim et al., a simple thermal treatment removes the PS microdomains.[67]

3.2. Morphology of Thin Films

When a block copolymer is confined to form a thin film on a surface, the microdomain morphology is critically influenced both by the film thickness and by the energetics of interaction at the air/polymer and polymer/substrate interfaces.[88−94] In general, interfacial energies will differ for blocks of different chemical composition. This leads to preferential wetting of each interface by selective blocks of the copolymer. For example, lamellar microdomains of symmetric PS-*b*-PMMA deposited on the native oxide surface of a silicon wafer are oriented parallel to the surface with PMMA wetting the substrate surface while PS lamellae assemble at the air interface. This is due, respectively, to the affinity of the polar PMMA block for the hydrophilic oxide surface and the lower surface energy of the nonpolar PS block. This ordering behavior of PS-*b*-PMMA films on a selective substrate (silicon wafer with native oxide) has been studied extensively by Russell and co-workers using secondary ion mass spectroscopy (SIMS), interference microscopy, and neutron reflectivity (NR).[88] Figure 12 shows a schematic representation, depth profile of SIMS, and interference microscopy, which indicate the parallel orientation of lamellar microdomains on the substrate.

This preferential wetting has important consequences. For PS-*b*-PMMA, if the film thickness is commensurate with the block-copolymer periodicity, L_0, then a series of lamellae of alternating composition join the two interfaces. When the mean film thickness is incommensurate with the periodicity [e.g., for PS-*b*-PMMA, thickness $\neq (n + 1/2)L_0$], the periodicity of diblock copolymer microdomains results in generation of very unique topography on the surface of block copolymer thin films. Often called islands and holes, these features form on the surface to minimize the total energy by quantizing the local film thickness. The schematic drawing in Figure 12 depicts an island (or a hole) formation in PS-*b*-PMMA as well.

When the thickness of the block copolymer film is below L_0, more complicated ordering is exhibited. In this case, the formation of lamellar microdomains parallel to the surface would incur entropic penalty as the molecules would be forced into compressed microdomains. Such constrained systems sometimes adopt a morphology where lamellar microdomains are oriented perpendicular to the surface. Such ordering behavior is particularly interesting as it can provide nanoscale patterns on the surface of substrates. We will discuss this morphology in greater detail in the following section.

3.3. Thickness-Dependent Nanopatterning

We indicated that thickness is a key factor that determines the morphology of block copolymers in thin films. It is

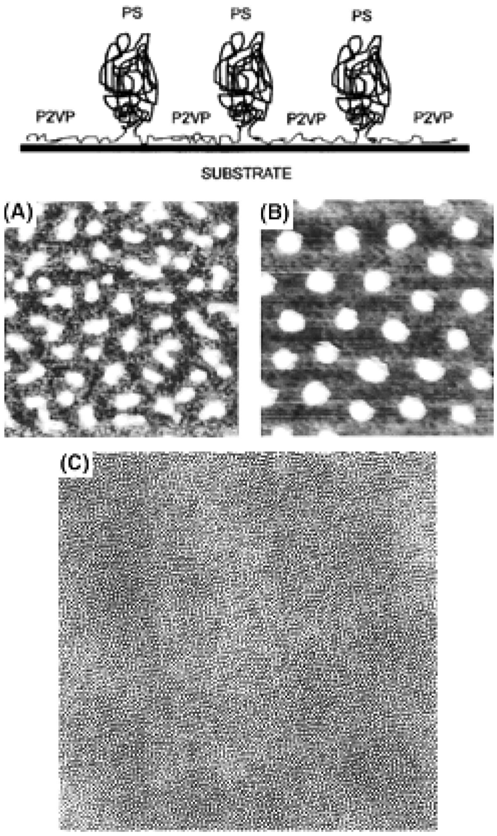

Figure 13. (Top) Schematic representation of surface micelles of PS-*b*-P2VP. (Bottom) Scanning force micrographs of ultrathin PS-*b*-P2VP films: (A) directly after spin coating (length of the image corresponds to 550 nm), (B) after annealing (length of the image corresponds to 550 nm), (C) large-scale image of the same film as shown in B (length of the image corresponds to 11 μm). (Reprinted with permission from ref 96. Copyright 1997 American Chemical Society.)

convenient, therefore, to categorize the formation of such nanostructures based on thicknesses of the block-copolymer films.

3.3.1. Ultrathin Films: Monomolecular Films

In this category, the nominal film thickness is much less than the natural period L_0. Möller and co-workers reported the microphase separation and self-ordering behavior of block copolymers under conditions where the surface concentration is below that necessary to form a continuous monomolecular layer.[95−101] Submonomolecular-thick films were formed by spin coating or dip coating 0.01−0.1 mg/mL solutions of poly(styrene-*b*-2-vinyl pyridine) (PS-*b*-P2VP) in chloroform onto mica substrates. At such high dilutions no micelle association can be expected in the solvent. Figure 13 displays surface force micrographs and the authors' schematic representation of the proposed arrangement. Annealing for 24 h at 150 °C considerably improves the ordering. Clusters 5 nm in height are separated by a rather smooth, 1 nm thick layer. The spacing of the pattern is about 100 nm, rather large for the molecular weight of block copolymer used. Using X-ray photoelectron spectroscopy (XPS) data, they demonstrated that such extensive stretching of the poly(2-vinylpyridine) (P2VP) chains is due to strong interactions between pyridine units and the substrate. By varying the molecular weight of the block copolymer, the PS clusters can be spaced on a 70−400 nm lateral period, with heights of 3−12 nm and diameters of 30−160 nm.

Lateral placement of the PS cluster in ultrathin films of poly(styrene-*b*-hydroxystyrene) (PS-*b*-PHOST) has been reported recently.[102] As shown in the AFM image in Figure 14a, positioning of the clusters could be directed by a topographic pattern on a silicon substrate. Monte Carlo simulation results (shown in Figure 14b) provide guidance in selecting proper dimensions required to locate a single cluster on each topographic pattern.

3.3.2. Sub-L_0 Thick Films

This category includes films whose thickness ranges from those just able to form a continuous layer to those approximately L_0 in thickness. Within this range, both experimental and theoretical results indicate a complex morphology of block copolymers. Here the driving force to form microdomains at L_0 competes with surface interactions to produce frustrated morphologies; slow phase separation kinetics add further complication. Morkved and Jaeger observed a morphological change from lamellar domains paralleling the substrate to perpendicular domains as the film thickness varies within this range.[103,104] The perpendicular orientation arises only at a thickness of one lamellar repeat spacing and low annealing temperature. As shown in Figure 15a, they observed perpendicular domains when a symmetric PS-*b*-PMMA (molecular weight of 65 500 g/mol) thin film of thickness L_0 was annealed at 155 °C. Figure 15b shows coexisting morphologies in a film with a thickness gradient. The film structure varies from long continuous strips to short discontinuous strips to disordered, isolated PMMA domains as the thickness ranges over the interval from 1/2 L_0 to 3/2

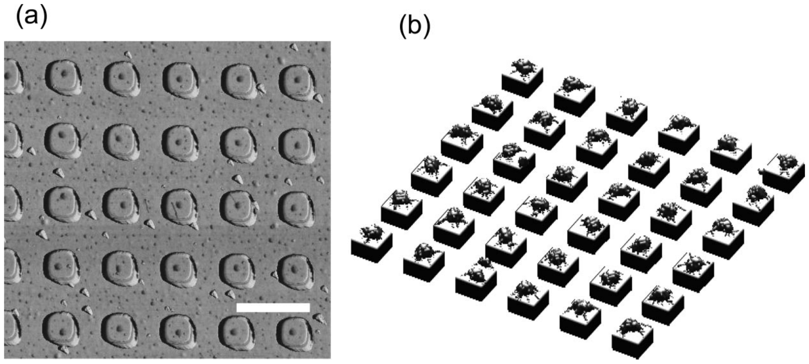

Figure 14. (a) Tapping mode AFM image of ultrathin PS-*b*-PHOST films formed on topographic patterns (scale bar, 1 μm). (b) Monte Carlo simulation results of micelles positioning on the mesa array. (Reprinted with permission from ref 102. Copyright 2007 Wiley-VCH Verlag GmbH & Co. KGaA.)

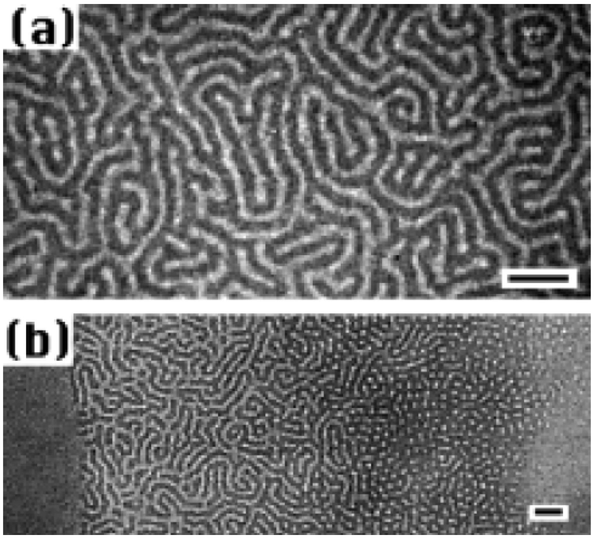

Figure 15. TEM micrographs of the perpendicular lamellar morphology of PS-*b*-PMMA. Light domains correspond to PMMA and dark domains to PS. (a) Uniform film thickness $t = L_0$. (b) Coexisting morphologies in a film with thickness gradient spanning the range $t \approx 3/2\ L_0$ (left) to $t \approx 1/2\ L_0$ (right). The size bar in both images indicates 100 nm. (Reprinted with permission from ref 103. Copyright 1997 EDP Sciences.)

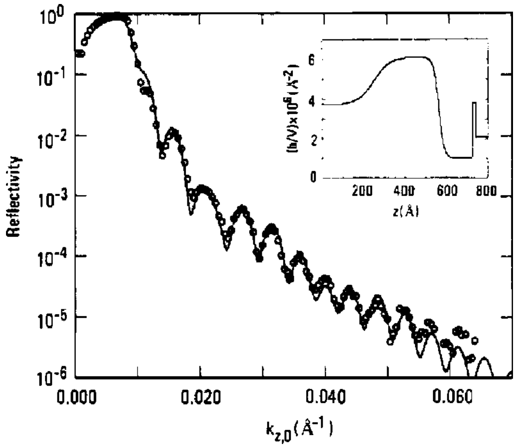

Figure 16. Neutron reflectivity profile for a film of PdS-*b*-PMMA that is L_0 thick. The circles represent the measured profile, whereas the solid line was calculated by using the scattering length density (SLD) profile shown in the inset. (Reprinted with permission from ref 105. Copyright 1991 American Chemical Society.)

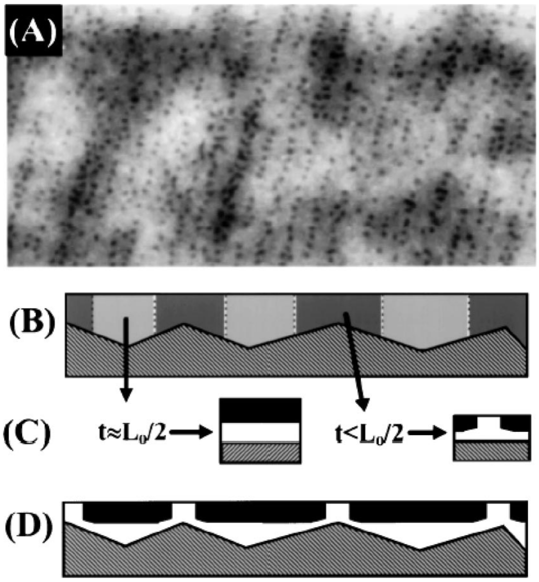

Figure 17. (A) AFM of diblock film morphology on corrugated substrates. This image is 5 μm × 2.5 μm. (B−D) Diagrams illustrate why the lateral patterning occurs. (Reprinted with permission from ref 106. Copyright 1997 American Physical Society.)

L_0. The authors suggested effective confinement, where phase separation occurs well before thickness quantization, as a possible mechanism for this behavior.

Such unconventional morphology of thin films of PS-*b*-PMMA had been reported previously by Russell and co-workers.[105] Using X-ray photoelectron spectroscopy (XPS) and neutron reflectivity (NR) to examine films of thickness L_0, they detected a phase-mixed morphology atop an underlying layer of PS and PMMA, demonstrating a marked perturbation of the morphology of the diblock copolymer from that usually observed in thin multilayer films and in the bulk (Figure 16).

Fasolka et al. studied the morphology of symmetric diblock-copolymer films of poly(styrene-*b*-*n*-butyl methacrylate) (PS-*b*-P*n*BMA).[106,107] In the thickness regime below $L_0/2$, they found a film morphology characterized by the formation of uniformly sized lateral domains and symmetric wetting. They also observed that when such films were prepared on substrates with surface corrugation, local variations in film thickness caused the formation of nanoscopic patterns. As shown in Figure 17, uniformly sized lateral domains are located on top of the ridges of the corrugated surface.

More systematic theoretical and experimental analyses of the morphological behavior of diblock copolymer thin films at thicknesses below L_0 have been reported. Figure 18 displays morphologies in cross section and an example phase diagram predicted by a series of self-consistent field (SCF) calculations.[107] As this figure illustrates and experimental work further demonstrates, confinement of block copolymer films within this thickness range affects both domain formation and domain orientation and thus surface patterns.

Earlier we noted that exposure of block copolymer thin films to solvent vapor offers an alternate means to influence ordering under dynamic nonequilibrium conditions. The ordering and/or orientation of microdomains are sensitive to the nature of solvent and to such experimental parameters as exposure time, temperature, and evaporation speed. Han and co-workers systematically studied the thin film morphology of symmetric PS-*b*-PMMA thin films annealed in solvent vapors with varying selectivity.[108−110] The solvent selectivity is characterized by the value of polymer−solvent interaction parameter, χ_{PS}, as calculated from Flory−Huggins solution theory using the equations

$$\chi_{PS} = V_S(\delta_S - \delta_P)^2/rT + 0.34 \text{ for nonpolar systems}$$

or

$$\chi_{PS} = V_S[(\delta_{dS} - \delta_{dP})^2 + (\delta_{pS} - \delta_{pP})^2]/rT \text{ for polar systems}$$

where V_S is the molar volume of the solvent, r is the gas constant, T is the absolute temperature, δ_S and δ_P are, respectively, the solubility parameters of the solvent and polymer, δ_d is the dispersion solubility parameter, and δ_p is the polar solubility parameter. By that theory, polymer and solvent are completely miscible over the entire composition range when $\chi_{PS} < 0.5$. Acetone ($\chi_{PS} = 1.1$ for PS and 0.29

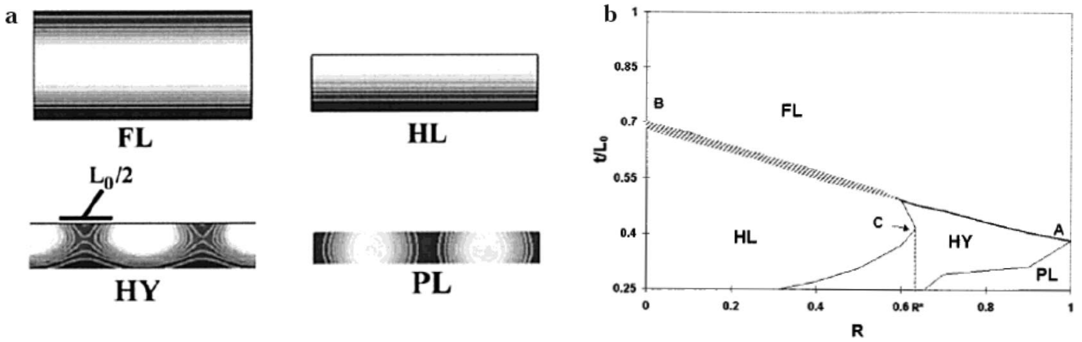

Figure 18. (a) Summary of morphologies illuminated by the SCF calculations. The morphologies are shown in cross section with abbreviations as follows: FL = full surface-parallel lamellae, HL = surface-parallel half-lamellae, HY = hybrid structure, PL = perpendicular lamellae. Black indicates 100% B segments and white 100% A segments. (b) Example phase diagram. $R = S^2_B/S^1_B$, where S^2_B and S^1_B are attractive interactions between B segments and film/substrate and film/air interfaces, respectively. Phase fields are labeled with the abbreviations found in a. (Reprinted with permission from ref 107. Copyright 2000 American Chemical Society.)

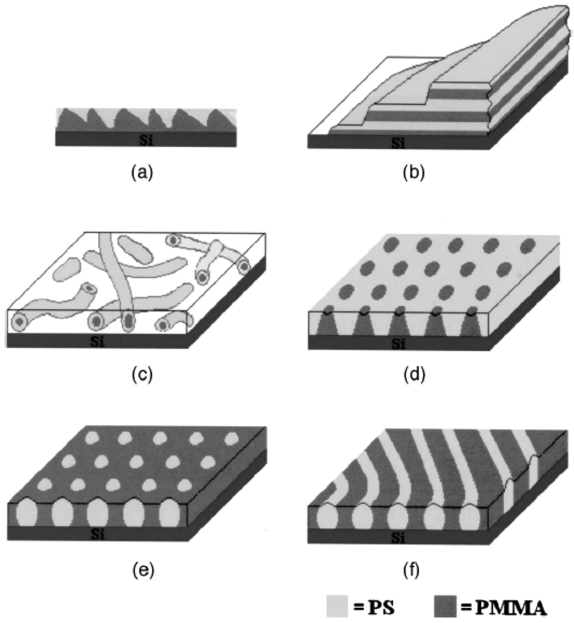

Figure 19. Schematic representation of the PS-*b*-PMMA morphology of as-cast film and subsequently annealed under different solvent vapors: (a) As-cast film, (b) exposed to tetrahydrofuran (THF), (c) exposed to CS_2, and (d−f) exposed to acetone with increasing exposure time. (Reprinted with permission from ref 109. Copyright 2004 American Institute of Physics.)

for PMMA) and carbon disulfide (CS_2, $\chi_{PS} = 0.43$ for PS and 1.2 for PMMA) were chosen as selective solvents for PMMA and PS, respectively. Tetrahydrofuran (THF, $\chi_{PS} = 0.34$ for PS and 0.88 for PMMA) was selected as a good solvent for both PS and PMMA. Quite different thin film structures were observed depending on the solvent selectivity, as schematically presented in Figure 19.[109] While a terraced morphology is observed with THF, a disordered micellar structure is seen with CS_2. Annealing under acetone leads to dewetting of the film to form fractal-like holes, with highly ordered nanoscale depressions in the still-wetted regions of the film. This evidence that solvent annealing can provide such nonequilibrium metastable structures offers the promise that still other interesting block copolymer thin film morphologies can be formed; this requires an improved understanding of how selectivity, vapor pressure, time, and temperature influence ordering behavior.

Russell and co-workers introduced a versatile approach to surface modification that greatly enhances orientation control of microdomains in diblock copolymer thin films.[111−116] Practically, this has been a breakthrough that has been incorporated into a wide range of schemes that apply block copolymers for nanofabrication. In their concept, precise control of the interfacial energy difference of a two-component system, such as an AB diblock copolymer, is achieved by end grafting a layer of an A−B random copolymer onto a surface, forming a random copolymer brush that presents an energetically *neutral interface* to the block copolymer film. If the grafting density is sufficiently high, then a polymer placed in contact with the modified surface interacts only with the brush. The interfacial energy of homopolymer A with the brush, γ_{Af}, decreases monotonically with increasing f, the A monomer fraction in the random copolymer brush. In the limit as the degree of polymerization $N \rightarrow \infty$, $\gamma_{Af} = (1 - f)\gamma_{AB}$ and $\gamma_{Bf} = f\gamma_{AB}$. Therefore, the interfacial energy difference, $\Delta\gamma = \gamma_{AB}(2f - 1)$, can vary from γ_{AB} at $f = 1$ to $-\gamma_{AB}$ at $f = 0$. At an intermediate value of f, $\Delta\gamma = 0$. Thus, by accurately controlling the composition of the random copolymer brush, a neutral surface can be realized. As shown in Figure 20, this concept was demonstrated using random copolymers of S and MMA that are anchored to the surface through hydroxyl end groups, where the interfacial energy of the random copolymer brushes with PS and PMMA are equal when f is about 0.6.[112]

The ordering behavior of symmetric PS-*b*-PMMA on a substrate coated with the neutral random copolymer brush was characterized using optical microscopy, NR, and small angle neutron scattering (SANS). This analysis shows a mixed morphology where lamellae adjacent to the free surface are oriented parallel to the plane of the film, while those lamellae adjacent to the substrate are oriented normal to that plane. Figure 21 shows optical micrographs of PS-*b*-PMMA films on Si substrates coated with random copolymers of PS and PMMA.[113]

The neutral interface has been put to use to control cylindrical microdomains of PS-*b*-PMMA as well. The nanoscopic templates generated by cylindrical pores in thin block copolymer films (illustrated in Figure 22) open up a variety of candidate applications in nanofabrication.[85]

3.3.3. Thick Films

Block-copolymer films potentially can provide high aspect ratio templates for many practical applications. Such use requires preparation of films typically hundreds of nanometers to micrometers thick, much greater than L_0, with controlled orientation of microdomains. Thus far, the major-

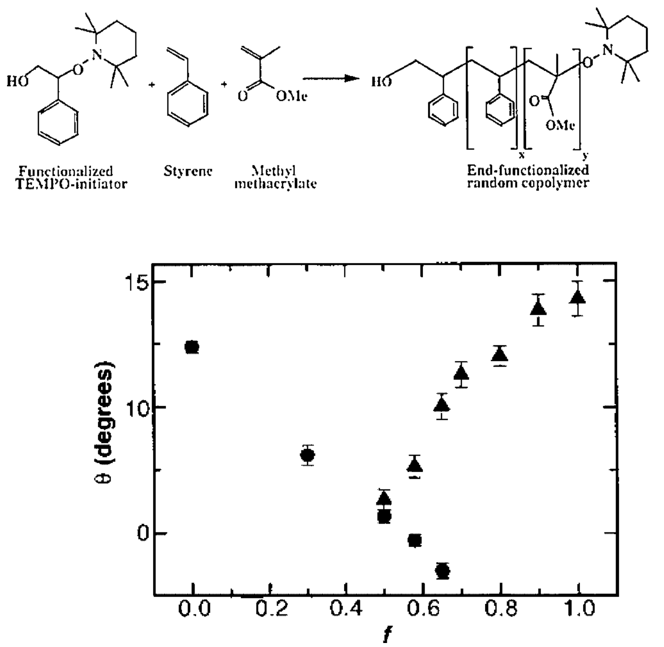

Figure 20. (Top) Synthetic scheme for PS-*r*-PMMA. (Bottom) Contact angles (θ) for PS (circles) and PMMA (triangles) on PS-*r*-PMMA brushes as a function of f in the random copolymer. (Reprinted with permission from ref 112. Copyright 1997 American Association for the Advancement of Science.)

ity of studies aimed at this purpose have used cylindrical microdomains to fabricate templates with nanopores accessible from the air interface. Russell and co-workers demonstrated one effective means to direct the orientation of cylindrical domains perpendicular to the surface in thick films by applying a DC electric field (30−40 V/μm) while heating the block copolymer film above its glass transition temperature (schematic in Figure 23).[117] The authors prepared nanopore arrays in approximately 1 μm thick PS-*b*-PMMA films and used electroplating to form within the pores vertical arrays of Co or Cu nanowires at areal densities in excess of 1.9×10^{11} wires per square centimeter.

Recently Steiner and co-workers reported a similar approach to prepare nanoporous templates using electric field alignment of cylinders formed in films of poly(4-fluorostyrene-*b*-D,L-lactide) (PFS-*b*-PLA).[117] The PFS-*b*-PLA system is amenable to processing under mild chemical conditions: the minority PLA component can be removed by hydrolytic degradation with dilute aqueous base, and the PFS pattern can be stripped by simple solvent dissolution or UV irradiation. They demonstrated the generation of freestanding copper oxide nanowire arrays using electrodeposition and subsequent removal of the PFS template. As shown in Figure 24, the method for template removal influences the structural stability of the freestanding array: the wires bunch together with solvent dissolution, whereas the UV treatment leads to less clustering of the wires. A similar effect (line collapse) is observed when

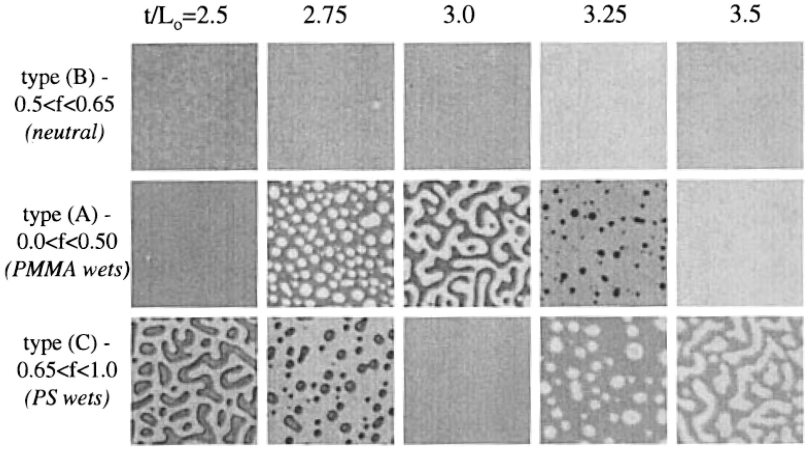

Figure 21. Reflection optical micrograph of PS-*b*-PMMA films on Si substrates coated with PS-*r*-PMMA brushes. The film thicknesses in each column are identical, and only the composition of the anchored brush is changed. The film thickness increases from ~2.5 L$_0$ to ~3.5 L$_0$ from left to right. (Reprinted with permission from ref 113. Copyright 1997 American Chemical Society.)

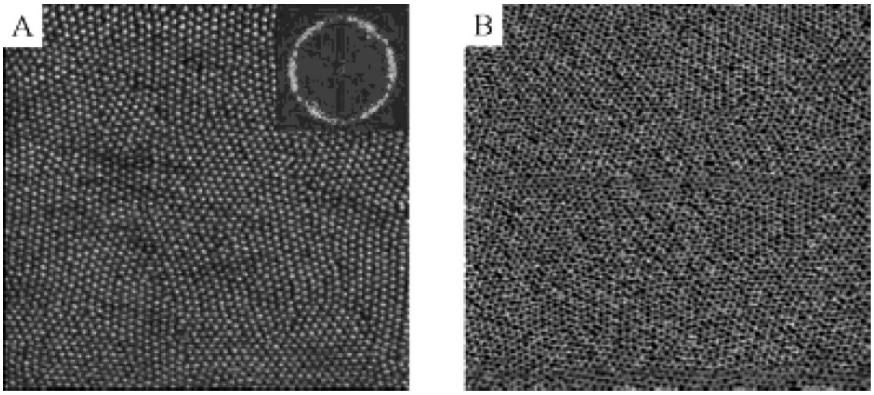

Figure 22. Phase contrast AFM images of nanoporous templates. (A) Surface of PS-*b*-PMMA ordered on the anchored random copolymer brush. (Inset) 2D FFT of the image. (B) After selective removal of PMMA domains by UV exposure and acetic acid rinsing. The size of the images is 2×2 μm^2. The z range of phase data is 5° and 35°, respectively. (Reprinted with permission from ref 85. Copyright 2001 Wiley-VCH Verlag GmbH & Co. KGaA.)

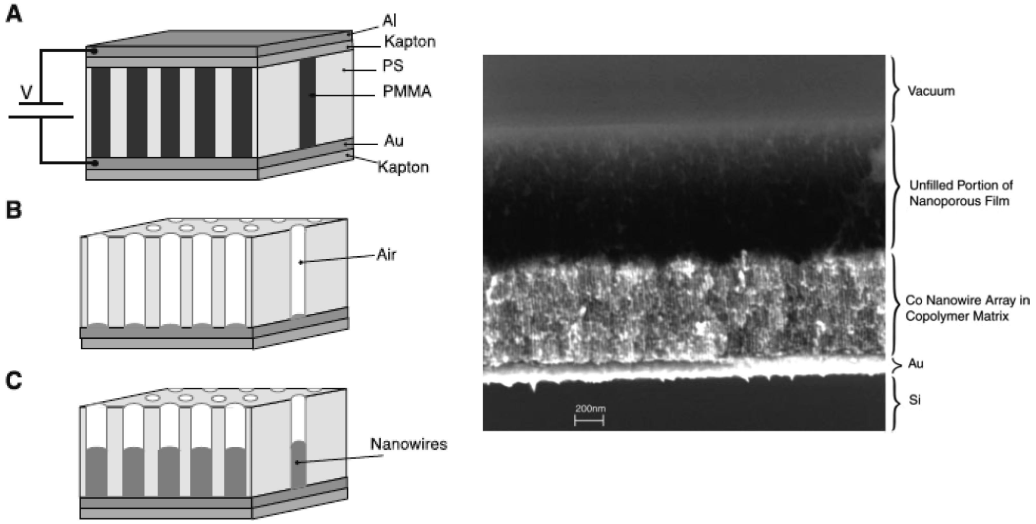

Figure 23. Schematic representation of high-density nanowire fabrication in a polymer matrix. (A) An asymmetric diblock copolymer annealed above the glass transition temperature of the copolymer between two electrodes under an applied electric field, forming a hexagonal array of cylinders oriented normal to the film surface. (B) After removal of the minor component, a nanoporous film is formed. (C) By electrodeposition, nanowires can be grown in the porous template, forming an array of nanowires in a polymer matrix. (Reprinted with permission from ref 117. Copyright 2000 American Association for the Advancement of Science.)

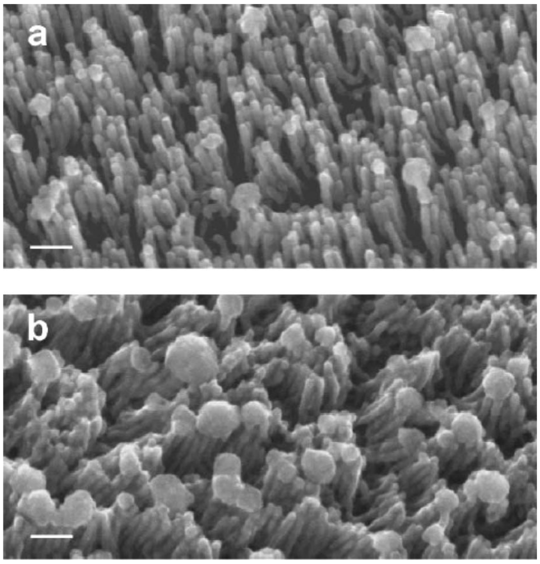

Figure 24. SEM images of (a) free-standing, electrodeposited nanowires following UV degradation of the PFS matrix and (b) free-standing wires following solvent dissolution of the PFS matrix in toluene. The PFS-*b*-PLA template was aligned using an electric field strength of 155 V μm^{-1}. The scale bar represents 100 nm. (Reprinted with permission from ref 118. Copyright 2007 The Royal Society of Chemistry.)

high-aspect nanoscale features are formed in photoresist films during pattern development and is attributed to surface tension effects during the final drying step.[118]

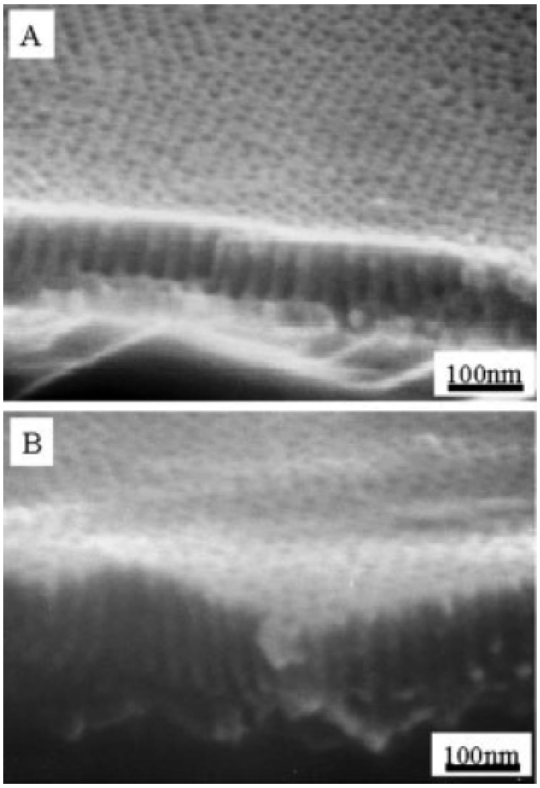

Figure 25. Cross-sectional SEM images for mixtures of PS-*b*-PMMA/PMMA with a PMMA fraction of 0.26: (a) 92 nm thick, (b) 329 nm thick film. PMMA phases were removed using UV irradiation. (Reprinted with permission from ref 120. Copyright 2004 Wiley-VCH Verlag GmbH & Co. KGaA.)

Addition of PMMA homopolymer to an asymmetric PS-*b*-PMMA has been shown to improve the persistence of orientation of cylindrical PMMA microdomains perpendicular to the surface, thereby enabling formation of high aspect ratio cylindrical microdomains in thick films of the mixture. Jeong et al.[120] studied thick films of a combination of asymmetric PS-*b*-PMMA and PMMA on a surface neutralized using a random PS-*r*-PMMA copolymer. Examining the case where the PMMA homopolymer comprises a fixed amount (26%) of the mixture, they found that a perpendicular orientation of cylindrical microdomains can be maintained to a maximum thickness ($H_{\max}$) that increases as the magnitude of the ratio of the molecular weights of PMMA to that of the PMMA block in PS-*b*-PMMA increases. In another case, where the molecular weight of PMMA was held equal to that of PMMA block, $H_{\max}$ increased from about 110 nm to about 340 nm when the amount of homopolymer was raised from 15% to 33%. Figure 25 shows cross-sectional scanning electron microscopy (SEM) images of 92 and 273 nm thick films that were prepared by adding 26% of PMMA to PS-*b*-PMMA.

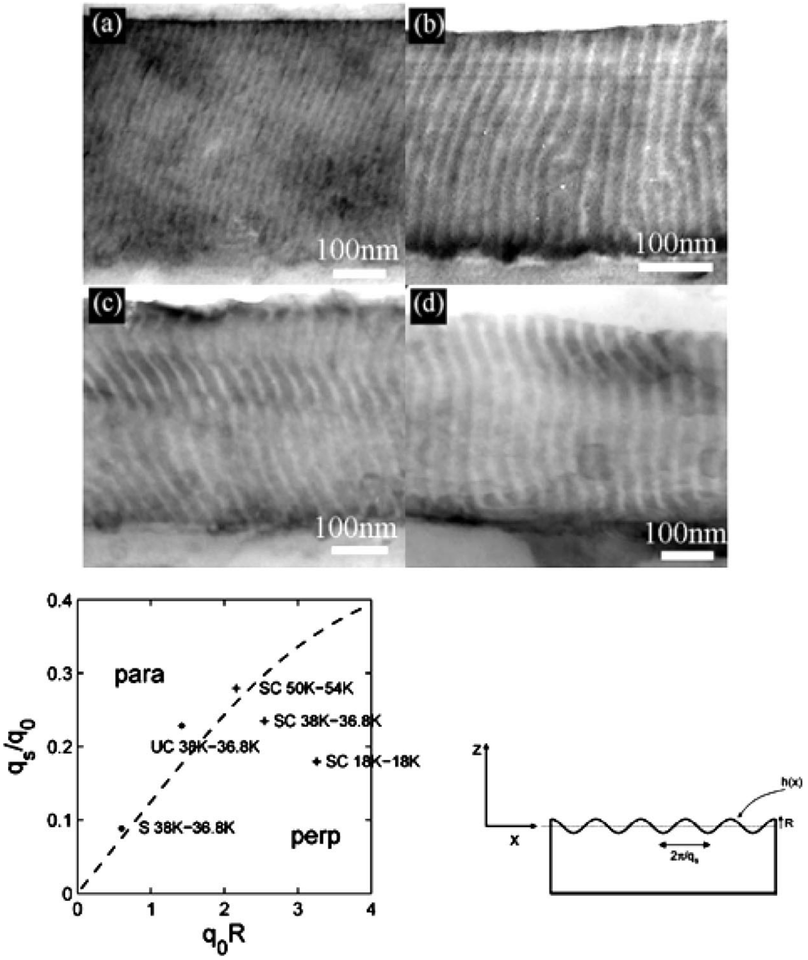

Figure 26. (Top) Cross-sectional TEM images of various molecular weight PS-*b*-PMMA thin films annealed at 230 °C on indium tin oxide surface: (a) 18K−18K, (b) 38K−36.8K, (c) 38K−36.8K, and (d) 50K−54K annealed for 18, 5, 18, and 25 h, respectively. (Bottom left) Comparison between the model and experimental phase diagram for the perpendicular and parallel lamellar configurations on a rough substrate. The dashed line is transition based on calculation. R and q_s are scaled by q_0, the lamellae wavenumber. The "+" data points correspond to observed perpendicular morphology, while the "●" ones correspond to parallel lamellae. (Bottom right) Schematic illustration of the rough confining surface. (Reprinted with permission from references 123, 124. Copyright 2005 American Chemical Society.)

The texture of a substrate can be used to control the orientation of microdomains perpendicular to the surface. Sivaniah et al. reported the formation of perpendicularly oriented lamellar microdomains in 300−400 nm thick films (about 7.5−10 times L_0) of PS-*b*-PMMA applied to glass coated with indium tin oxide (ITO), a substrate with random roughness.[121−124] The roughness inhibits the growth of substrate-directed parallel lamellar formation; when conjoined with a neutral air/film interface the effect directs the lamellae into a perpendicular orientation. The cross-sectional TEM images in Figure 26(top) demonstrate that this phenomenon is general over a range of PS-*b*-PMMA molecular weights. The authors propose a simple model to explain the orientation transition of a block copolymer in contact with a rough substrate. Figure 26 (bottom left) compares an experimental phase diagram and their model, which describes the rough surface with a single one-dimensional corrugation mode (shown schematically in Figure 26 (bottom right)). The parameters q_s and R are the wavenumber and amplitude of the surface roughness, respectively. This simple description suggests that the orientation of microdomains on a rough surface is governed by the scaling parameters of surface roughness (expressed by q_s and R) and by the wavenumber of the bulk lamellae $q_0 = 2\pi/L_0$.

Drawing on the experience using multilayer resists in photolithography,[125] the combination of a thin imaging layer (in this case a block copolymer film) and an anisotropic image transfer process technology such as plasma etching can offer a facile route to high aspect ratio nanoporous templates.[126] An example is shown in Figure 27, where a bilayer scheme is used to form the nanoporous structure. Here a block copolymer thin film incorporating one domain with high resistance to an oxygen plasma etch (in this case an OS) is applied on top of a polymer underlayer which is readily etched. Upon plasma treatment the OS domains in the block copolymer film form a refractory oxide that acts as an etch mask, while the organic microdomains (i.e., PS in Figure 27) and the underlayer in the unprotected areas are eroded. A cross-sectional SEM image in Figure 27 shows high aspect ratio pores approximately 15 nm in diameter.

A rapid and an effective route to effect the orientation of cylindrical microdomains in thick films is through application of the solvent vapor treatment described earlier in this review. Lin et al. reported perpendicular orientation of cylindrical PEO domains when PS-*b*-PEO films were prepared on silicon substrates at a thickness several times the value of L_0.[127] Figure 28a shows an AFM phase image of such a spin-coated film.[128] Such ordering behavior under nonequilibrium conditions can be explained by formation of

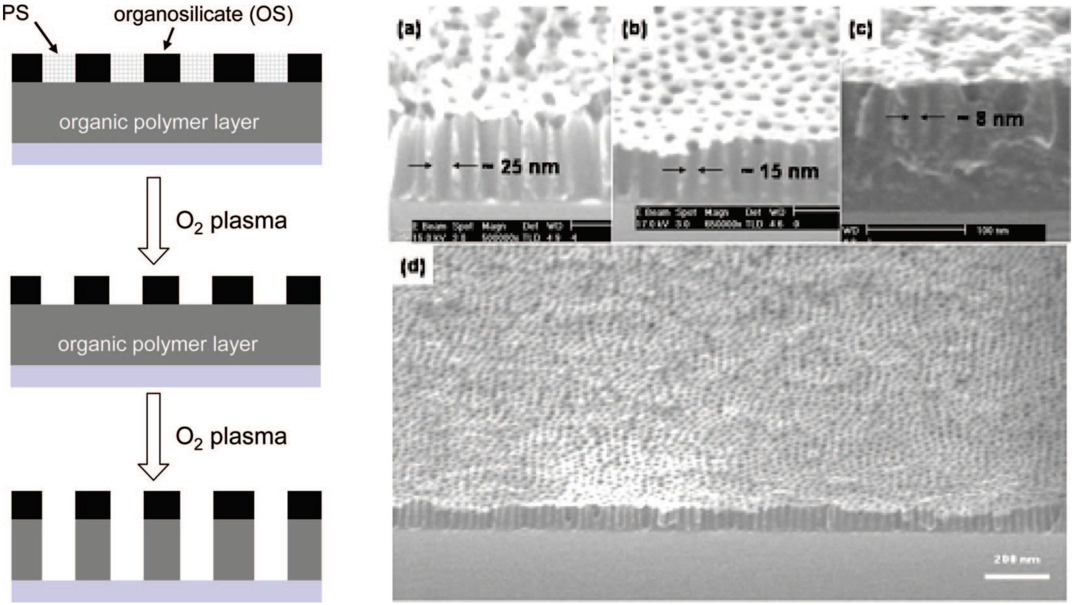

Figure 27. (Left) Schematic presentation of the process steps. (Right) Cross-sectional SEM images of the nanoporous template with pore diameters of (a) 25, (b) 15, and (c) 8 nm. (d) Tilted SEM image of the nanoporous tempate generated on a 5 in. silicon wafer (pore diameter ≈15 nm). (Reprinted with permission from ref 126. Copyright 2008 Wiley-VCH Verlag GmbH & Co. KGaA.)

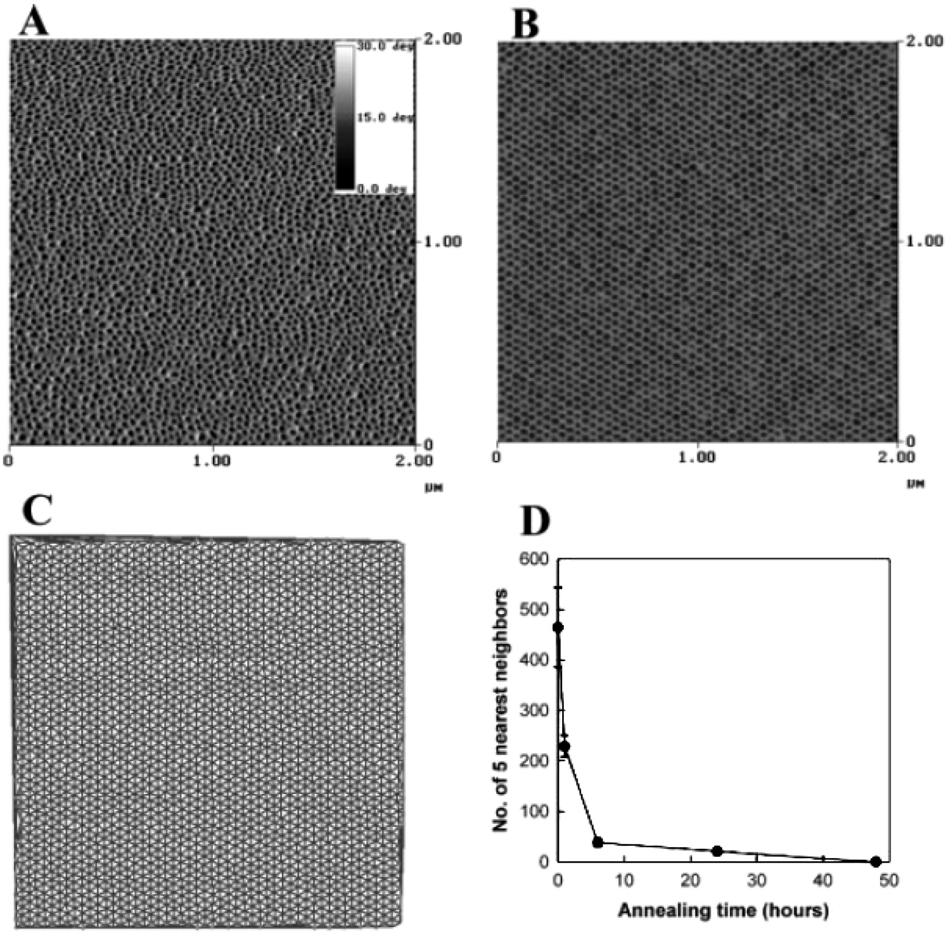

Figure 28. (a) PS-*b*-PEO thin film obtained by spin coating and (b) after annealing for 48 h in a benzene vapor, (c) triangulational image of the AFM image in b, and (d) the number of five-neighbor defects as a function of annealing time. (Reprinted with permission from ref 128. Copyright 2004 Wiley-VCH Verlag GmbH & Co. KGaA.)

a concentration gradient of solvent within the film during spin coating. The same group demonstrated remarkably improved long-range order of domains using postannealing of similar films under solvent vapor. As shown in Figure 28b, 28c, and 28d, a 48 h anneal of PS-*b*-PEO in an atmosphere containing benzene vapor removes defects and yields highly ordered arrays of cylindrical microdomains.[128]

This postannealing not only increases the lateral order of microdomains but also influences their orientation on the substrate. Figure 29 illustrates an example where the orienta-

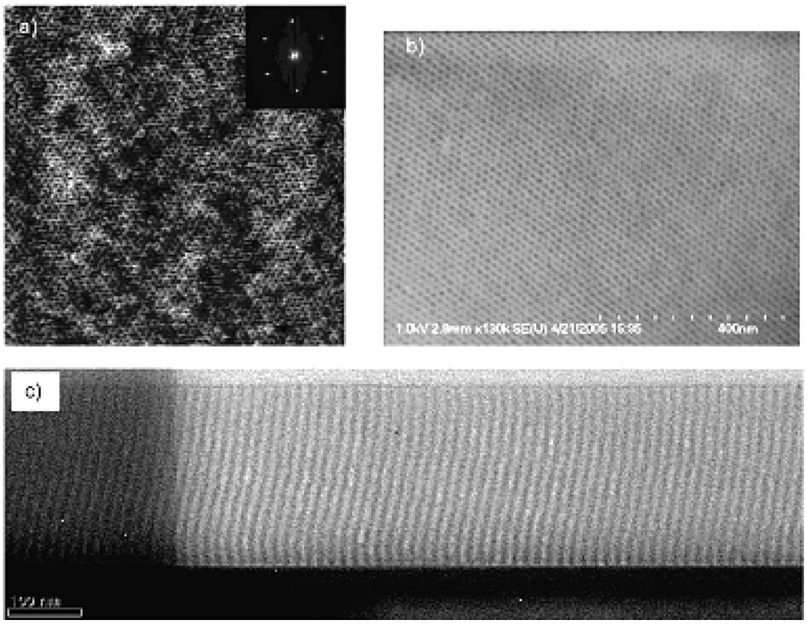

Figure 29. Perpendicular orientation of cylindrical pores after annealing for 48 h in a chloroform + octane vapor at 20 °C: (a and b) 1 μm × 1 μm height contrasted AFM image (10 nm height scale) and SEM micrograph of the surface. PS-*b*-PEO with a MW of 8600 g/mol was used. The inset in a is the Fourier transform of the AFM image. (c) TEM cross-sectional micrograph of the porous film shown in a and b. The darker and brighter regions correspond to SSQ and cylindrical pores, respectively. The film thickness is ~250 nm. (Reprinted with permission from ref 66. Copyright 2005 American Chemical Society.)

tion of cylindrical domains in a PS-*b*-PEO/OS hybrid system is controlled using solvent vapor.[66] The nature of the microdomains depends on careful selection of the solvent or solvent mixture.

3.4. Placement Control: Directed Self-Assembly (DSA)

While some applications of block copolymer thin films are tolerant of disorder and defects, the ability to precisely control the placement of microdomains on substrates greatly expands their range of practical uses. Numerous routes to control lateral order have been examined in depth experimentally at two distinct spatial scales: large-scale order over many periods and localized control over a distance of only a few periods. Collectively, these are approaches for effecting directed self-assembly (DSA). Typically, lithographically predefined structures (either topographic relief structures or chemically differentiated surface regions) are used to control placement. DSA has been demonstrated for a range of microdomain morphologies, from spheres to cylinders to lamellae, with each targeted at specific potential applications. We review several common DSA methods in this section.

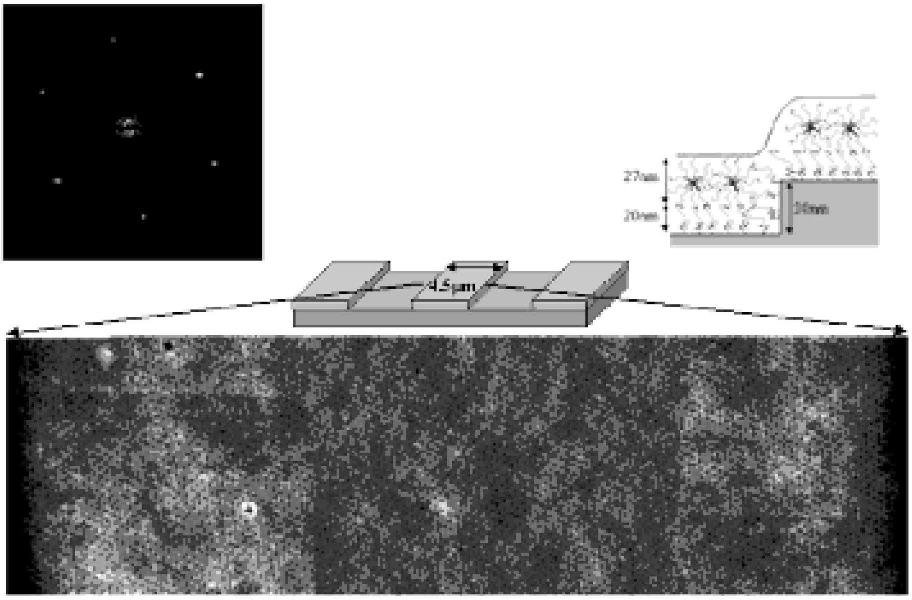

Figure 30. SFM of PS-*b*-PVP film on top of a mesa. When the mesa edges are less than 5 μm apart, a single crystal is formed. (The horizontal lines of imperfection indicate places where 1 μm × 1 μm SFM images were "sewn" together in order to create a large image with high resolution.) The six diffraction peaks in the associated FFT indicate that the grain is ordered in a single crystal with hexagonal symmetry. As illustrated in this schematic, a poly(vinyl pyridine) (blue) brush is observed on all SiO_2 surfaces (green) followed by a layer of spheres encased in a styrene matrix (red). (Reprinted with permission from ref 129. Copyright 2001 Wiley-VCH Verlag GmbH & Co. KGaA.)

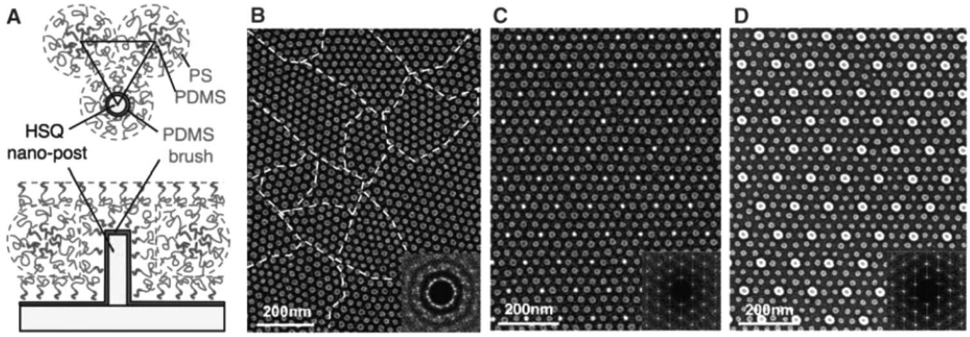

Figure 31. (A) Top-down and side-view schematic showing the arrangement of PS-*b*-PDMS block-copolymer molecules in the region surrounding a single post made from cross-linked HSQ resist. The post and substrate surfaces have been chemically functionalized by a monolayer of short-chain PDMS brush. (B) SEM images of a poorly ordered monolayer of BCP spherical domains formed on a flat surface, that is, without templating. The boundaries between different grain orientations are indicated with dashed lines. (Inset) 2D Fourier transform of the domain positions that shows the absence of long-range order. (C and D) SEM images of ordered BCP spheres formed within a sparse 2D lattice of HSQ posts (brighter dots). The substrate and post surfaces were functionalized with a PDMS brush layer in C, which corresponds to the schematic in A, and with a PS brush layer in D. (Insets) 2D Fourier transforms in which the low-frequency components originate from the post lattice. (Reprinted with permission from ref 138. Copyright 2008 American Association for the Advancement of Science.)

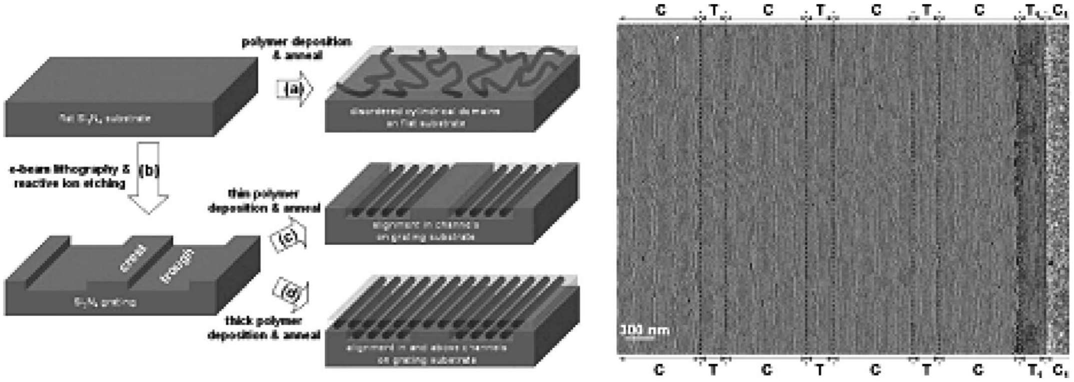

Figure 32. (Left) Schematic illustration of the strategy used to fabricate parallel arrays of aligned diblock-copolymer cylindrical domains. (a) Thin film of diblock copolymer spin coated and annealed on a flat substrate forms disordered cylindrical domains. (b) Grating patterns were prepared on a flat Si_3N_4 substrate by e-beam lithography and reactive ion etching. (c) A lower coverage of polymer on a patterned substrate, after annealing, forms aligned cylindrical domains parallel to the trough edges in the confined volumes of the troughs. (d) For a higher coverage of polymer, alignment in the troughs induces alignment above and beyond the confined volumes of the troughs. (Right) Large-scale alignment of cylinders. Phase AFM image, 3.8 μm × 5.2 μm. This sample was prepared on a substrate with 95 nm deep troughs and annealed at 130 °C for 30 h. Alignment of underlying cylinders in the troughs not only induces alignment of cylinders above the troughs but also aligns a single layer of cylinders on the crests. The troughs (T) have an 11/2 L_0 thick film, and the crests (C) have a 3/2 L_0 thick film. The trough marked T_1 has a 9/2 L_0 thick film, and the crest marked C_1 has an 1/2 L_0 thick film; therefore, this crest appears featureless. (Reprinted with permission from ref 133. Copyright 2004 American Chemical Society.)

3.4.1. Topographic Guiding Patterns: Graphoepitaxy

Surface relief structures can influence the assembly of microdomains of block copolymers.[129−140] Such topographic guiding patterns are commonly fashioned by plasma etching of solid substrates (e.g., a silicon wafer) using a patterned photoresist layer as an etch mask or by directly utilizing the photoresist image in those instances where it is not soluble in the block copolymer's casting solvent. Segalman et al. reported applying this graphoepitaxial strategy to generate arrays of spherical domains of PS-*b*-P2VP over large areas and with a high degree of perfection.[129] They found that while thin films of PS-*b*-P2VP deposited on a flat substrate show polycrystalline structure with a grain size of ca. 400 nm after thermal annealing, deposition of such films on a substrate patterned with mesas and wells leads to the formation of a single-crystal grain over large areas of the patterns. Figure 30 shows an array of spherical domains that extends between the edges of the mesa, a length of at least 4.5 μm. With this approach the width of the mesa and the well is found to more strongly influence the ordering than their heights. As the epitaxial growth is nucleated at the edges of the mesas, the center of the stripe tends to revert to the polygrained structure when the width of the mesa exceeds 5 μm.

A more systematic investigation of the ordering of spherical microdomains confined in lithographically defined grooves has been reported by Cheng et al. using a poly(styrene-*b*-ferrocenyldimethylsilane) (PS-*b*-PFS).[130−132] Using grooves with uniform and modulated widths, they were able to discern how elastic strain in the array of domains governs their local arrangement within the grooves.

Recently, Ross and co-workers reported an elegant experiment demonstrating the use of topographic structures to control self-assembly of spherical microdomains of poly(styrene-*b*-dimethylsiloxane) (PS-*b*-PDMS).[138] In this work, they applied the copolymer film to a substrate surface decorated with a regular array of discrete posts. The posts interact both locally and globally with the spherical domains, providing periodic constraints that drive the formation of a two-dimensional periodic nanostructure array with precisely determined orientation and long-range order. Figure 31 shows a schematic presentation of this technique and SEM images of ordered block copolymer domains that result from its application. With this *sparse template* approach, the com-

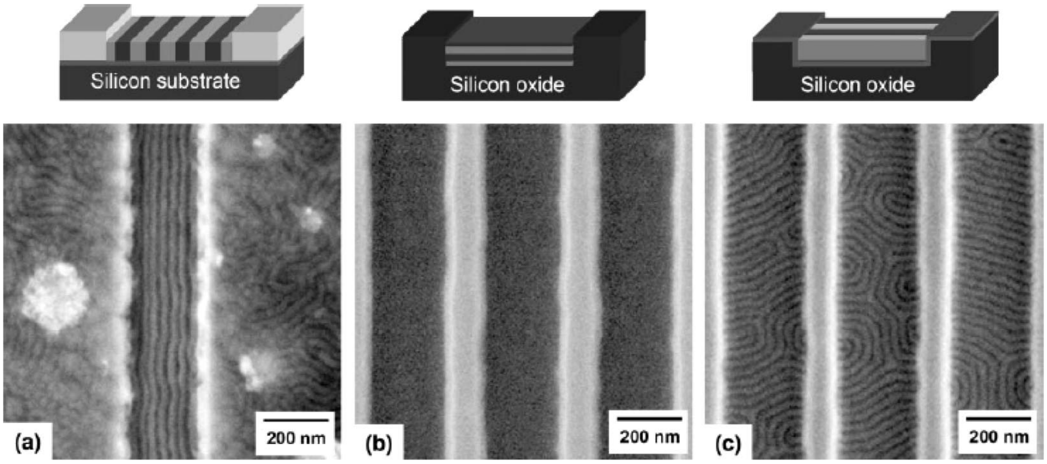

Figure 33. Lamellar structures of symmetric PS-*b*-PMMA (36 kg mol^{-1}) on topographically patterned substrates. (a) The side walls of the gold patterns (right and left) are preferentially wetted by the PS block. The bottom of the groove (middle) exhibits neutral wetting behavior to both blocks. (b) Lamellar structures are oriented parallel to the SiO_2 bottom of the grooves (dark) within a patterned SiO_2 substrate (light). (c) The lamellar domains are oriented perpendicular to both the substrate and the groove side walls when the topographic pattern in b is uniformly treated with a neutral brush. (Reprinted with permission from ref 136. Copyright 2007 Wiley-VCH Verlag GmbH & Co. KGaA.)

mensurability between the block-copolymer period and the template period governs the orientation and periodicity of the resulting array of spherical domains and is accurately described by a free energy model.

A simple method for spatial alignment of cylindrical microdomains in topographic patterns has been reported by Sibener and co-workers.[133−135] Topographic grating patterns were generated on silicon nitride substrates by electron beam lithography and reactive ion etching (RIE). When a thin film of an asymmetric poly[styrene-*b*-(ethylene-*alt*-propylene)] (PS-*b*-PEP) is coated on the patterned surface, the cylindrical PS domains align in the recessed troughs. In thicker films the alignment in the recessed areas induces alignment of the microdomains on the raised crests. Figure 32 shows a phase contrast AFM image that reveals large-scale alignment of cylindrical domains using the topographic patterns. Aligned cylinders are observed on both troughs and crests as schematically illustrated in Figure 32d.

Lamellar microdomains with controlled orientation perpendicular to the surface attract particular interest since they offer a potential route by which block copolymers can form line/space patterns like those frequently encountered in integrated circuit designs but at dimensions well below those available by leading-edge optical lithography. Though cylindrical microdomains oriented parallel to the surface can also be used to create line/space patterns, lamellae microdomains are preferred due to their uniform cross-sectional profile and simpler plasma etching process. DSA of lamellar domains using topographic guiding patterns has been reported by several groups. For lamellar microdomains, wetting properties of the bottom and side walls of the trench (or trough, groove, or well) govern the alignment orientation. Park et al. demonstrated control of lamellar alignment by constructing topographic patterns with tailored wetting properties.[136] When the bottom surface of the trench is neutral to both PS and PMMA microdomains (Figure 33a), a side wall that is selectively wetted by one of the blocks serves to induce orientation of lamellar domains parallel to the side wall surface. Here the lamellar domains subdivide the lithographically defined guiding pattern, in effect increasing the spatial resolution of the line patterns. This approach has some drawbacks, however. A high defect density can result if the width of the groove is not commensurate with the periodicity of the block copolymer; thus, precise dimensional control of the topographic pattern (to a fraction of L_0) is required.[139,140] Since the lamellar domains follow the contour of the side walls, no significant improvement in edge roughness over that of the guiding pattern can be anticipated.

When both bottom and side wall surfaces are energetically neutral, the lamellar domains align perpendicular to both the substrate and the side walls (Figure 33c). The effect of side wall edge roughness is small for this alignment scheme, but a high number density of defects can be found in the middle of the groove if the width of the groove exceeds the natural grain size of the lamellar domains. Recently, perpendicular alignment of lamellar domains in a channel approximately

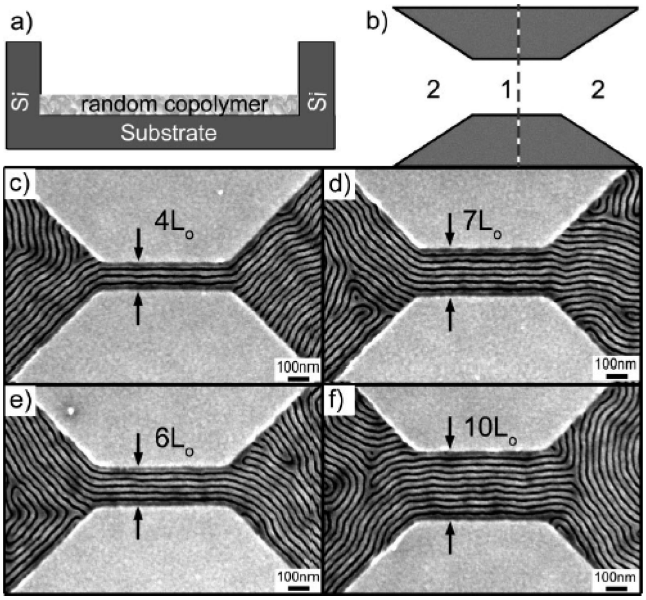

Figure 34. (a) Schematic representation of a trench cross-section prior to polymer deposition, taken along the dashed line shown in b. (b) Schematic representation of a fabricated silicon channel. White areas are recessed by ca. 20 nm with respect to the gray areas. (c−f) SEM images of trench widths ranging from 4 L_0 to 10 L_0, filled with defect-free lamellar striped patterns in registration with the trench walls within the narrow channel. Defects are excluded to the wider tapered zones. (Reprinted with permission from ref 137. Copyright 2007 Wiley-VCH Verlag GmbH & Co. KGaA.)

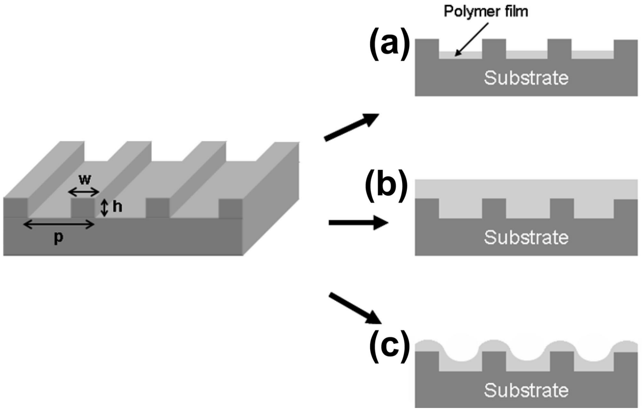

Figure 35. Schematic representation of the three thickness categories of block-copolymer film formation on topographic patterns: (a) block-copolymer thickness (t) < depth (h) of topographic guiding patterns; (b) $t > h$; (c) $t \approx h$. (Reprinted with permission from ref 142. Copyright 2009 The Royal Society of Chemistry.)

300 nm in width has been demonstrated by Park et al. using a block copolymer containing hybrid.[69]

Ruiz and co-workers reported on their efforts to control local defectivity by varying the geometry of the guiding pattern.[141] Referring to the schematic in Figure 34b, they constructed a tapered trench design that imposes a high free energy penalty for defect formation in the narrow trench (region 1) and promotes polymer shear flow such that defects diffuse to the wide areas (region 2) where the free energy cost is lower. Using this geometry, they demonstrated the formation of defect-free areas in channel widths up to 20 L_0 and lengths up to 5 μm, distances that far exceed the correlation length of this material in unconfined patterns.

Thus far we have described two distinct ways that surface topography can influence microdomain formation. In the first, the block copolymer film thickness is less than the depth of the topographic pattern; under this condition the copolymers are effectively confined in the channels of the patterns (depicted schematically in Figure 35a). In the second case, shown in Figure 35b, the thickness of the block copolymer film exceeds the height of the topography so that the underlying pattern creates thickness variations in the film, leading to localized formation of thickness-dependent morphologies. Relatively little attention has been devoted to a third regime where the film thickness is comparable to the pattern depth (Figure 35c). In this case, the block-copolymer film undulates along the contour of the substrate topography, and this influences microdomain formation. Kim and co-workers reported the alignment of the lamellar phase of a block-copolymer hybrid system on a corrugated surface (Figure 36).[15,70] Using a substrate patterned with a lithographically produced line grating, they observed that lamellae orient across the lines to yield a self-assembled crossbar nanostructure with lamellae of approximately 20 nm half pitch. The alignment of lamellae perpendicular to the direction of surface corrugation is believed to be due to differences in the bending properties of the aligned molecules along two axes, i.e., the width and length direction of the lamellae. Use of a hybrid material system adds some complexity to interpreting this effect, but a more recent report from the same group suggests that corrugation-induced orientation also can be achieved using a simple coil−coil diblock copolymer (PS-*b*-PMMA) when the proper length scale of surface corrugation and thickness of the polymer film are chosen.[142]

More recently, Park and co-workers reported the preparation of ordered arrays of cylindrical microdomains by depositing block copolymers on faceted surfaces of sapphire wafers.[143] They found the sawtoothed substrate topography provides

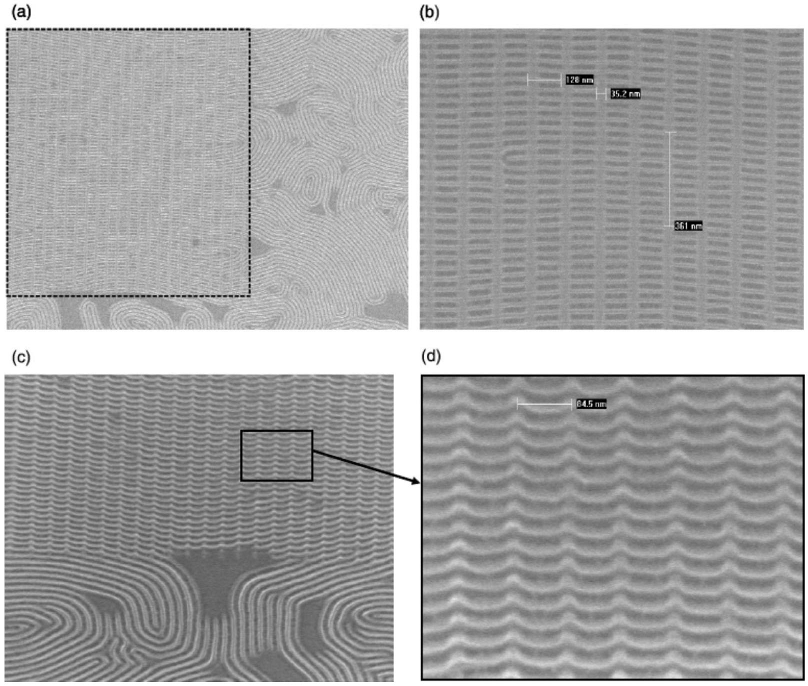

Figure 36. Plan-view SEM images of the lamellae on a substrate containing corrugated patterns. PS-*b*-PEO was removed by thermal treatment at 450 °C for 2 h. (a) Low-magnification SEM image. Randomly aligned lamellae are observed on the flat surface (right-hand side of the image). The lamellae on the corrugated area (within the dotted square) show alignment perpendicular to the direction of substrate corrugation (vertical lines in the image, $W = 35$ nm, $L = 126$ nm). (b) High-magnification SEM image of aligned lamellae. The horizontal and vertical lines are lamellae from the PS-*b*-PEO/PMS resin hybrid and substrate corrugation from e-beam lithography, respectively. (c) Tilted SEM image. Strong alignment of lamellae is observed on the corrugated area of the substrate ($W = 35$ nm, $L = 84$ nm). (d) High-magnification SEM image of figure c. The lamellae (horizontal lines) run over the substrate corrugation (vertical lines) and form a wave-like structure on the corrugated substrate. (Reprinted with permission from ref 70. Copyright 2008 IOP Publishing Limited.)

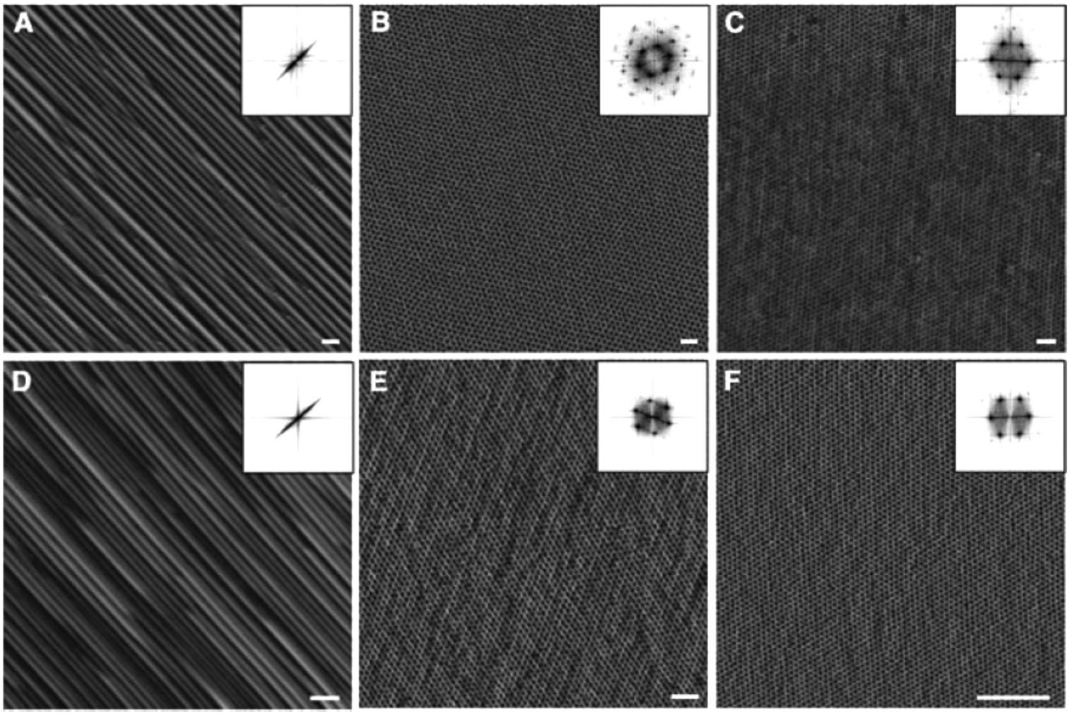

Figure 37. AFM height images of sawtooth patterns and phase images of solvent-annealed PS-*b*-PEO thin films. (A and D) When M-plane sapphire was annealed at 1400 and 1500 °C, a pitch of ~48 and ~24 nm and a peak-to-valley depth of ~6 and ~3 nm were obtained, respectively. Highly ordered PEO cylindrical microdomains having areal densities of 0.74−10.5 terabit/in.^{2} from PS-*b*-PEO (M_n = 26.5 kg/mol), (B) PS-*b*-PEO (M_n = 25.4 kg/mol), (C) PS-*b*-PEO (M_n = 21.0 kg/mol), (E) PS-*b*-PEO (M_n = 7.0 kg/mol), and (F) BCP thin films annealed in *o*-xylene vapor. Scale bars, 100 nm. (Reprinted with permission from ref 143. Copyright 2009 American Association for the Advancement of Science.)

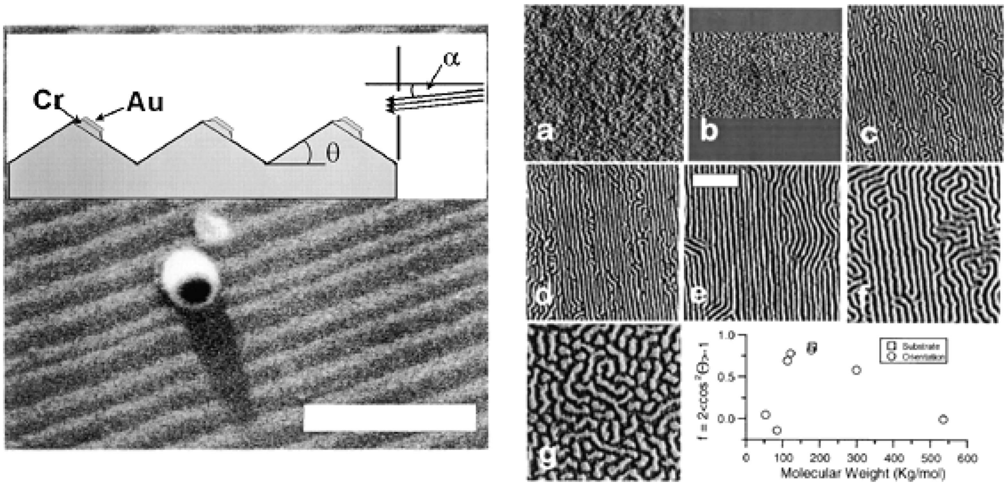

Figure 38. (Left) Field emission scanning electron micrograph of a periodic heterogeneous surface. The surface impurity was included within the micrograph to demonstrate the effects of shadowing. The average stripe period here is 105 nm, with a metallization line width averaging 55 nm. The scale bar shown is 0.6 μm. (Inset) Schematic diagram of the glancing angle evaporation geometry used. Provided the incidence angle α of the metal atoms is less than the apex angle θ of the facets, shadowing will occur and a heterogeneous surface will be produced. (Right) AFM tapping mode phase images of free surface of PS-*b*-PMMA films of a range of molecular weights, solution cast on a 60 nm heterogeneous substrate. Molecular weights (× 10^3 g/mol) [degree of commensurability *s*] are as follows: (a) 57 [0.48]; (b) 84 [0.61]; (c) 113 [0.74]; (d) 121.3 [0.78]; (e) 177 [0.99], (f) 300 [1.4]; (g) 535 [2.05]. The scale bar shown in e is 0.5 μm; same scale applies to all images. (Inset) Calculated 2D orientation function for each sample. (Reprinted with permission from ref 144. Copyright 1999 American Physical Society.)

directional guidance to the self-assembly of the block copolymer, which is tolerant of surface defects, such as dislocation. As shown in Figure 37, they could achieve the lateral ordering and lattice orientation of the single-grain arrays of microdomains over the entire surface.

3.4.2. Chemical Guiding Patterns: Chemical Epitaxy

We have seen how one can manipulate domain alignment by systematically varying the properties of selected surfaces within a topographic feature. This principle also has been extended to the planar case, where the patternwise introduction of chemical heterogeneity on the surface allows the energetics of the polymer−surface interaction to be controlled in a spatially localized way that directs the alignment of block copolymer domains. To be effective, the length scale of the surface heterogeneity must be close to that of the microdomain periodicity. Rockford et al. established a relationship between controlled nano-

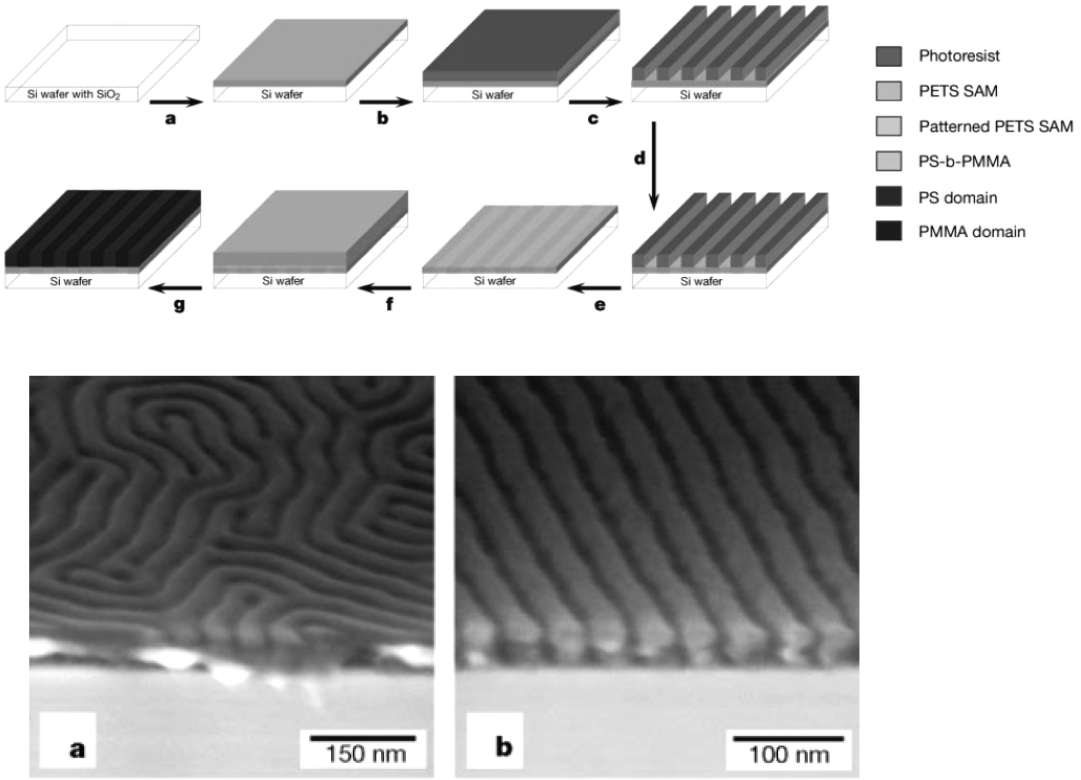

Figure 39. (Top) Schematic representation of DSA using chemical guiding patterns. (Bottom) Lamellar microdomains of PS-*b*-PMMA on (a) unpatterned and (b) patterned surfaces. (Reprinted with permission from ref 145. Copyright 2003 Nature Publishing Group.)

scale surface interactions and subsequent macromolecular ordering.[144] They used a surface striped with oxide and metal, as shown in Figure 38, where the stripe width is comparable to the size of a polymer molecule. Grooves with a lateral period of tens of nanometers and a height amplitude of several nanometers were prepared from single-crystal silicon wafers intentionally miscut at an angle from the crystal orientation. Consecutive evaporation of chromium and gold onto the surface at a glancing incidence angle α creates precise periodic chemical heterogeneity on the surface. Since PS preferentially interacts with a gold surface, distinctly different alignments of microdomains of PS-*b*-PMMA are observed as one varies the degree of commensurability *s* (defined as the ratio of block-copolymer period in the bulk to the substrate period). As shown in the right-hand side of Figure 38, the lamellae are oriented normal to the substrate surface and directed by the underlying strips on the heterogeneous surface.

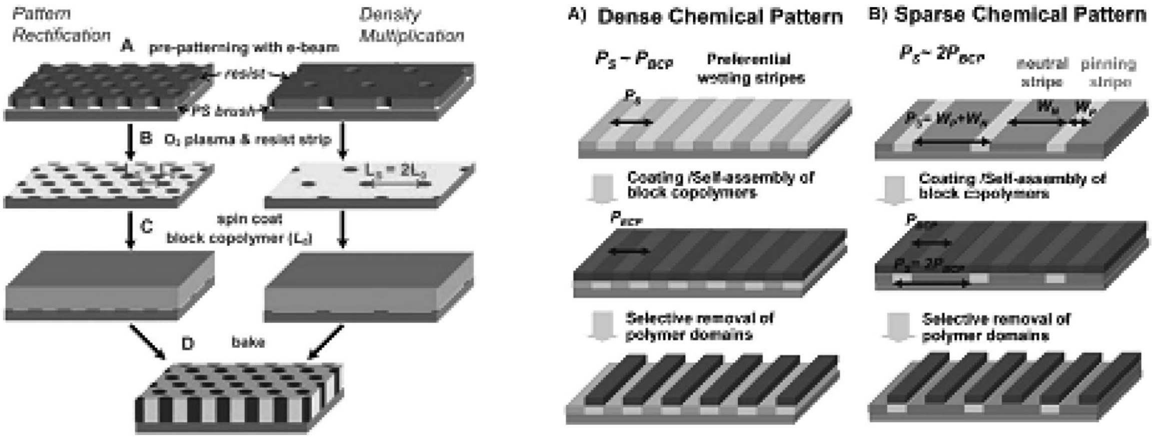

Figure 40. Process steps to create lithographically defined chemically prepatterned surfaces and subsequent directed assembly: (left) with cylindrical microdomains of block copolymers; (right) schematics of directed self-assembly of block copolymers with a natural period of P_{BCP} on chemical patterns. (A) Directed self-assembly based on dense chemical patterns of alternating preferential wetting stripes with a pitch of the patterned substrate (P_s) close to P_{BCP}. The affinity between chemical patterns and block-copolymer domains drives self-alignment of the block copolymer. Perfect pattern registration and reduced CD variation are the main advantages of this method. (B) Sparse chemical patterns comprised of alternating pinning stripes (width $= W_P = 0.5P_{BCP}$) and neutral stripes (width $= W_N = P_S - W_N$) with a pitch which is twice that of the block copolymers ($P_S/P_{BCP} \approx 2$). The self-assembled block copolymer doubles the spatial frequency of the underlying guiding chemical patterns. One domain of the block copolymers is selectively removed to show the self-assembled line-space patterns. (Reprinted with permission from refs 147 and 149. Copyright 2008 American Association for the Advancement of Science and Copyright 2008 Wiley-VCH Verlag GmbH & Co. KGaA.)

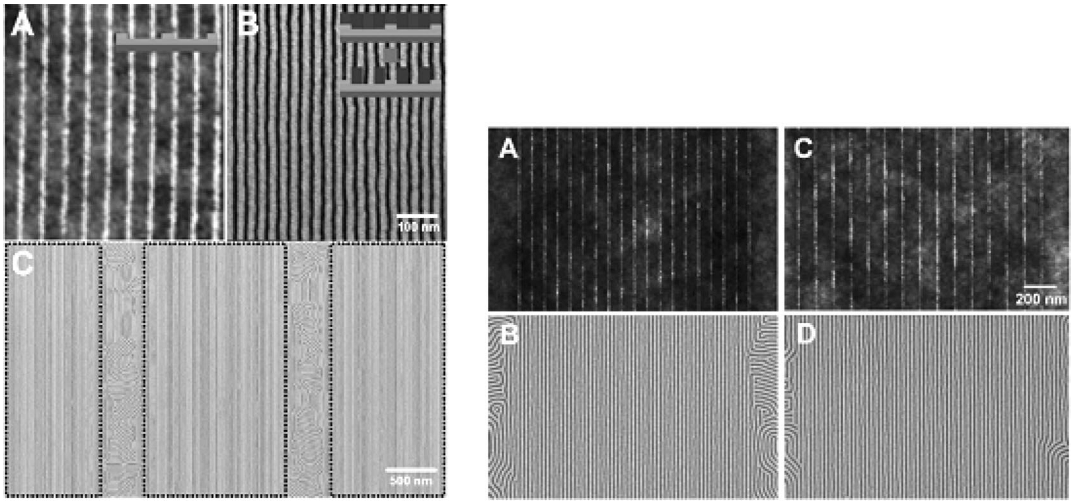

Figure 41. (Left) Sparse chemical patterns and frequency doubling of directed self-assembly of block copolymers on the chemical patterns. (A) Atomic-force micrograph (AFM) height image of stripes of e-beam resist on the neutral underlyaer with a pitch (P_s) 57.5 nm for guiding the self-assembly of PS-*b*-PMMA ($P_{BCP} \approx 28.5$ nm). (B) Scanning electron micrograph (SEM) of self-assembled PS-*b*-PMMA after removing PMMA using an oxygen plasma treatment. The remaining self-assembled lines double the spatial frequency of sparse chemical patterns shown in A. (C) Defect-free frequency doubling within the chemically patterned area (dotted frame). (Right) Frequency multiplication of resist patterns by directed self-assembly. The AFM height images show resist stripes on the neutral underlayer with a pitch of (A) 85 and (C) 115 nm. (B) SEM micrograph of the self-assembled lines with a pitch of 28.2 nm triples the spatial frequency of the resist pattern. (D) SEM micrograph of the self-assembled lines with a pitch of 28.8 nm quadruples the spatial frequency of the resist pattern. (Reprinted with permission from ref 149. Copyright 2008 Wiley-VCH Verlag GmbH & Co. KGaA.)

Nealey and co-workers introduced a lithographic technique for creating patterns with chemical contrast on substrates.[145-147] Figure 39 shows a schematic of their process, along with experimental images that depict alignment of the lamellar phase of PS-*b*-PMMA. Patterns of chemical contrast are formed on the substrate by preparing a thin film of polymer brush on the substrate, followed by extreme ultraviolet interferometric lithography to form the chemical pattern. Defect-free alignment of lamellar microdomains over large areas was achieved using this approach when the periodicity of the chemical patterns matches that of the lamellar microdomains of the block copolymer. This method has proved to be very effective; even complex pattern geometries containing bends, T junctions, and jogs have been generated.[146]

Recently, three groups independently reported examples of the rectification and multiplication of sparse, lithographically defined chemical surface patterns using DSA of block copolymers. The basic concept is depicted in Figure 40. While Ruiz et al.[147] and Tada et al.[148] formed cylindrical microdomains of PS-*b*-PMMA in their variants, Cheng and co-workers[149] tested their method using the lamellar phase of that material. The approach used by Cheng et al., shown in Figure 41, makes it possible to double, triple, and quadruple the spatial frequencies of surface chemical patterns using block copolymers. They also demonstrated self-healing behavior of the block copolymers on poorly defined chemical patterns, illustrating the beneficial rectifying effect of block copolymer self-assembly. This approach offers the potential to save significant time and effort when creating regular patterns over large areas.

3.4.3. Other DSA Methods

A number of other approaches have been proposed for potential application to DSA. Each approach has its strengths and shortcomings, and each requires more study prior to practical use as a patterning method. Li and Yokohama report a method called "soft-molding", which employs an elastomeric mold to align a single layer of cylindrical domains of a block copolymer thin film in a particular direction.[150] A schematic description of their approach is depicted in Figure 42 (top left). They obtained 3×10^5 parallel lines over an area of 1 cm^2 using a polydimethylsiloxane (PDMS) mold to align a poly(styrene-*b*-ethylene butylene-*b*-styrene) (SEBS) triblock copolymer.

Nanoimprint lithography was combined with PS-*b*-PMMA self-assembly by Li and Huck.[151] Using the block copolymer as a nanoimprint resist (Figure 42 (bottom left)) they demonstrated that, for both cylindrical and lamellar microdomains, the imprint template can add control of lateral placement of microdomains.

4. Applications to Nanofabrication

More than a decade ago, Mansky et al. demonstrated that the ordered periodic domains in a block copolymer thin film can be put to use as a patterning template.[152] This is analogous to the role that photoresist patterns play in traditional lithographic applications, but in this case the dimensional scale extends to a range not easily accessed by conventional optical lithography. Using poly(styrene-*b*-butadiene) (PS-*b*-PB), they investigated techniques for creating large-area patterns from a monolayer of spherical or cylindrical microdomains.

Since this seminal work, numerous reports have described processes wherein a pattern formed in a block copolymer thin film is replicated in the solid substrate by a subsequent image transfer step.[23,26,153,154] In one study by Park and co-workers at Princeton, dense periodic arrays

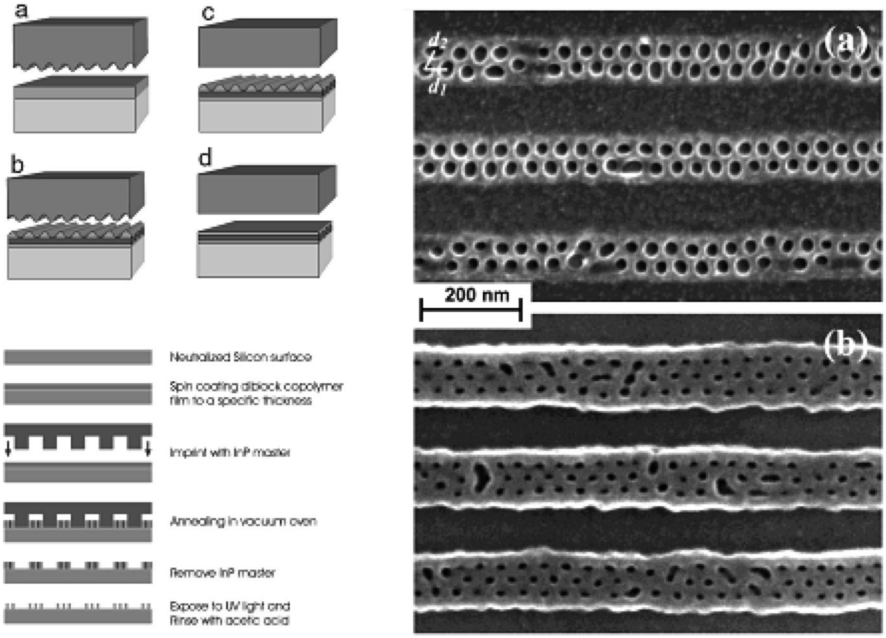

Figure 42. (Top left) Schematic illustrations of the soft molding process to align cylinders in a block-copolymer thin film. (a) A PDMS mold with a grating surface pattern was placed on the thin film and pressure was applied. (b) The grating pattern was transferred onto the surface of the copolymer film after annealing above its glass transition temperature (T_g). The cylinders of the block copolymer were aligned perpendicular to the grating ridges. (c) A flat PDMS mold was placed on the patterned thin film to recover a flat surface. (d) A flat thin film of the block copolymer with a single layer of cylinders perfectly aligned in a particular direction was fabricated. (Bottom left) Schematic diagram of procedures for controlled self-assembly nanolithography with block copolymers. (Right) SEM images of controlled self-assembled PS-*b*-PMMA diblock-copolymer structures with imprinted InP gratings of (a) 200 nm periodicity with about a 100 nm gap and (b) 210 nm periodicity with about a 120 nm gap. The PMMA columns are etched away in both samples. (Reprinted with permission from refs 150 and 151. Copyright 2005 Wiley-VCH Verlag GmbH & Co. KGaA and Copyright 2004 American Chemical Society.)

of holes and dots were fabricated on a silicon nitride-coated silicon wafer surface.[23,153] Figure 43 schematically depicts their approach. A uniform microdomain monolayer was prepared on the silicon nitride layer by controlling the thickness of the block copolymer film. The PB forms both spherical microdomains within the film and continuous wetting layers at the air and silicon nitride interfaces. Ozonation of the film preferentially erodes the PB microdomains to generate an array of holes in the polymer film, while treatment with osmium tetroxide leads to selective reaction of the oxidant with the PB microdomains to form an array of metal-containing etch-resistant spheres. When post-treated with a fluorine-based RIE process, these structures produce arrays of holes or dots, respectively, in the substrate's silicon nitride surface.

The combination of semiconductor processing technologies such as RIE with block copolymer nanopatterning opens new possibilities for fabricating nanostructures useful for functional devices. A recent article reviews this topic in depth.[26] Here we summarize several illustrative examples. In these examples the aim has been to utilize the self-assembly of block copolymer based nanostructures to carry out a single critical step of a complex integration scheme rather than the fabrication of an entire device.

4.1. Interconnects: Air Gap Fabrication

In one early application, block-copolymer nanostructures are combined with semiconductor fabrication technology to fabricate "air-gap" structures. These structures are intended for future integrated circuit designs to be incorporated in the wiring layers that interconnect individual transistors. The time delay in such interconnections is a performance-limiting factor, and the limitation grows more severe as feature size is scaled down. The interconnection time delay is dependent upon two factors: the resistance of the metal wire conductor, and the capacitance associated with the dielectric medium that surrounds the conductor.[155] Replacement of aluminum conductors with copper reduces the *RC* (resistance × capacitance) delay by approximately 35%. If the silicon dioxide insulator (which has a dielectric constant of 4) can be replaced with air (dielectric constant of ∼1) the *RC* delay can be reduced by a further 75%. Hence, there is much interest in devising methods for controllably forming an air gap between metal interconnect lines. IBM has explored the application of block copolymer nanostructures to fabricate air-gap structures. Figure 44 schematically illustrates the process sequence.[156] An organic diblock copolymer with cylindrical morphology was used to form dense via-like nanopatterns atop a hard mask silicon oxide layer. To ensure that the cylinders for the minority phase were oriented vertically, the silicon oxide layer was first coated with a random brush polymer layer engineered to have the same affinity for both blocks of the diblock polymer. The diblock material was formulated such that the areal density and the hole diameters of the final pattern and the material etch properties were well suited for the following image transfer step. After diblock deposition, the minority phase was selectively etched away and the resulting holes replicated in the hard mask layer using an RIE step. A coarse lithographically defined "block out mask" was applied to selectively protect certain regions from further etching, and the nanoperforations were then transferred into the wiring level where the silicon oxide-based insulator was eroded to form the air gap. The narrow openings initially

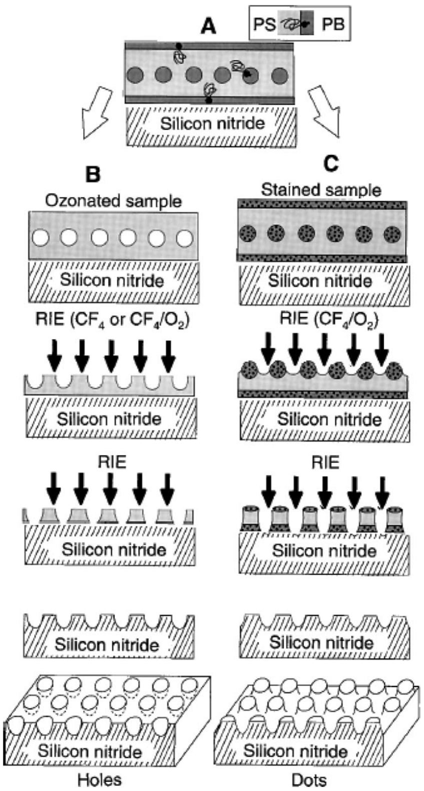

Figure 43. (A) Schematic cross-sectional view of a nanolithography template consisting of a uniform monolayer of PB spherical microdomains on silicon nitride. PB wets the air and substrate interfaces. (B) Schematic of the processing flow when an ozonated copolymer film is etched, which produces holes in silicon nitride. (C) Schematic of the processing flow when an osmium-stained copolymer film is etched, which produces dots in silicon nitride. (Reprinted with permission from ref 23. Copyright 1997 American Association for the Advancement of Science.)

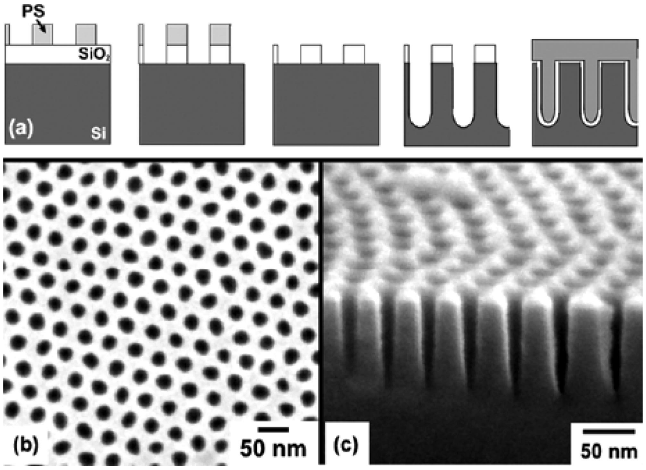

Figure 45. (a) Schematic process flow for decoupling capacitor fabrication. (b) Top-down SEM image of porous oxide hard mask. Pore diameters are 20 nm with center-to-center spacing of 40 nm. (c) 70° angle SEM image of MOS capacitor bottom Si electrode. Pores etched to a depth of 100 nm. (Reprinted with permission from ref 158. Copyright 2004 IEEE.)

formed using the block copolymer film template are readily sealed in a final deposition step, leaving the circuit with a close to planar surface ready for the next layer. Performance modeling indicates that the expected capacitance gain is 35%, and this was routinely observed by in-line measurements. One advantage of this technology is a lower cost compared to other subtractive air-gap schemes.

4.2. Capacitors

As microelectronic devices are scaled, the fabrication of on-chip capacitors emerges as an issue. From elementary physics, when the dimensions of a capacitor are decreased, its capacitance is reduced. The design challenge is providing sufficient capacitance for proper circuit operation while conserving on-chip real estate. Black et al. reported the use of a diblock copolymer thin film for fabricating metal-oxide semiconductor (MOS) capacitors with increased charge storage capacity.[157,158] The authors

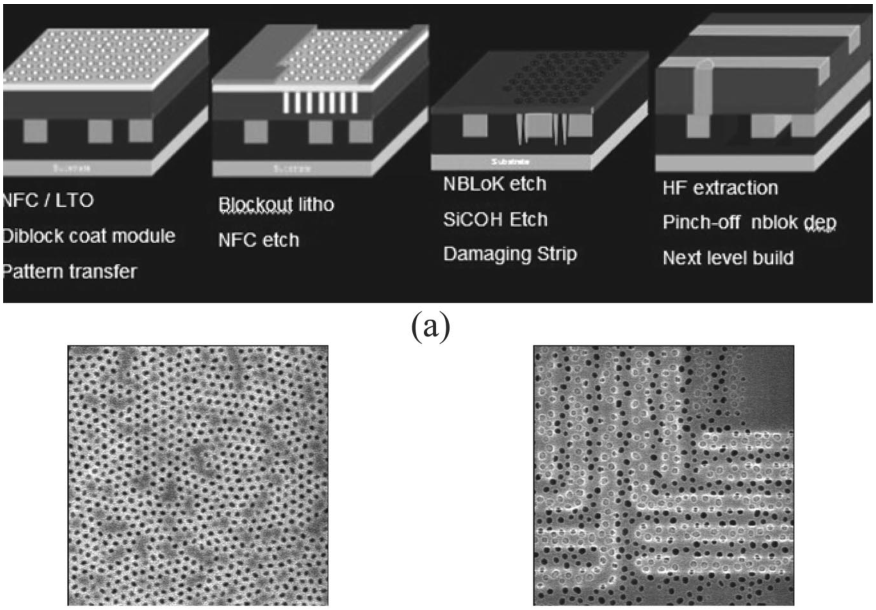

(a)

(b)

(c)

Figure 44. (a) Process sequence for fabricating air-gap structures using self-assembly. (b) Example of diblock self-assembly on a 300 mm wafer. (c) Representative top-down picture of a wiring macro after air-gap formation. (Reprinted with permission from ref 156. Copyright 2008 The Electrochemical Society.)

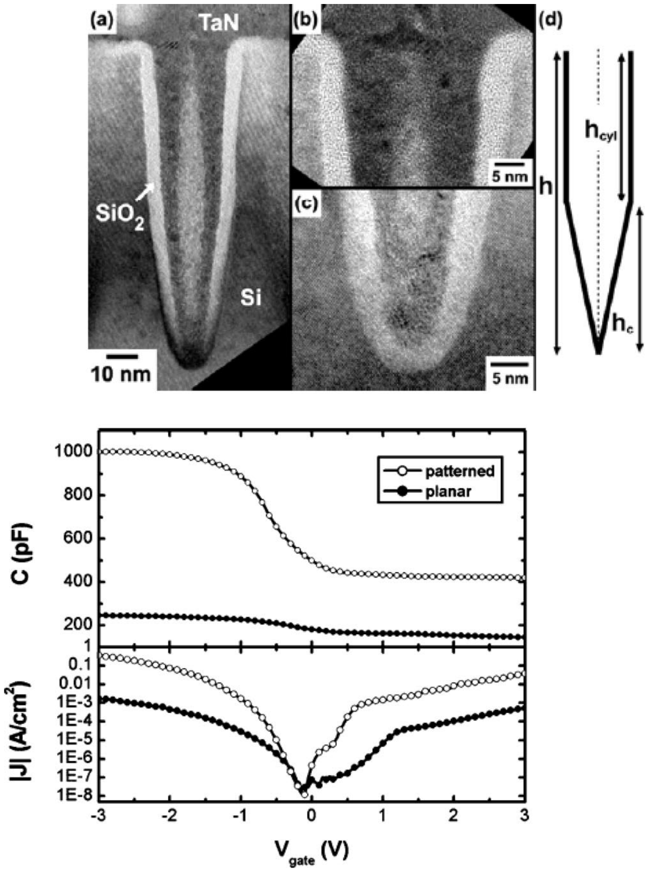

Figure 46. (Top) (a−c) Cross-section TEM images of completed MOS decoupling capacitor. (d) Schematic device cross section showing etch profile. (Bottom) (a) Capacitance versus voltage for planar (solid circles) and patterned (open circles) devices of the same lateral area (measured at 100 kHz). (b) Leakage current per lateral device area for planar (solid circles) and patterned (open circles) devices. (Reprinted with permission from ref 158. Copyright 2004 IEEE.)

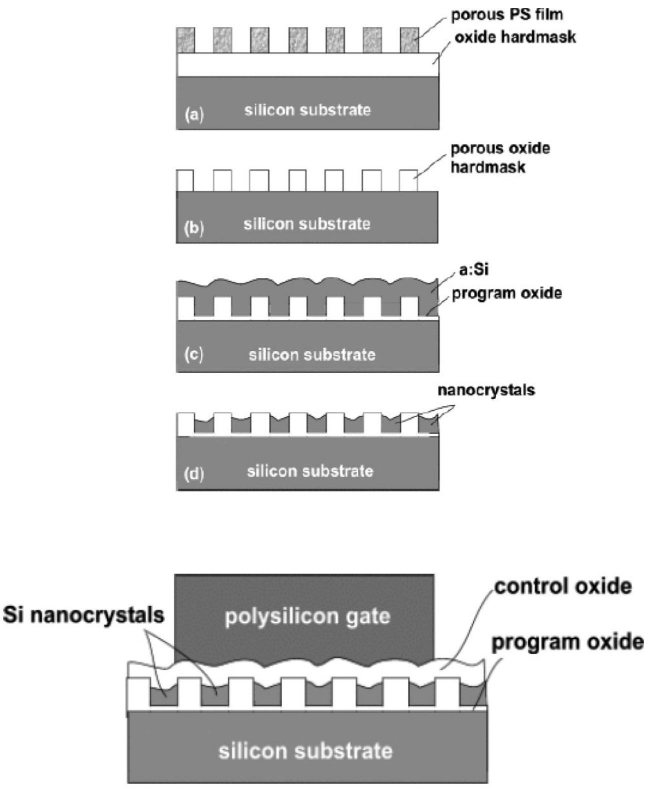

Figure 47. (a−d) Schematic diagrams of the process flow used to create an array of Si nanocrystals beginning with a porous self-assembled polymer template. (Bottom) Schematic diagram of the fabricated nanocrystal memory device. (Reprinted with permission from ref 159. Copyright 2003 IEEE.)

prepared a porous PS template by selectively removing cylindrical domains of PMMA from a film of asymmetric PS-*b*-PMMA (Figure 45). This template was used to pattern a silicon dioxide layer which in turn served as a hard mask for patterning the underlying silicon by RIE. The oxide mask is resistant to standard hydrogen bromide-based silicon gate etch chemistry, allowing the formation of a vertical profile. The MOS capacitor is completed by deposition of a top metal gate. The silicon nanopores are difficult to fill using standard metal physical vapor deposition techniques due to the narrow diameter and high aspect ratio, so atomic layer deposition was employed to coat tantalum nitride conformally on the oxide within the nanopores. Figure 46 shows cross-sectional TEM images of the completed MOS capacitors and their electrical characteristics.

4.3. Memory

The fabrication of a silicon nanocrystal floating-gate memory where block copolymer self-assembly is used to define the dimensions, density, and uniformity of the nanocrystals has been demonstrated by Guarini and co-workers.[159] As in the previous example, a porous PS film was formed by removing cylindrical PMMA domains from a thin film of PS-*b*-PMMA (see schematic in Figure 47). This film served as a sacrificial layer to define nanocrystals at sublithographic dimensions. After transferring the PS pattern through an underlying oxide layer, a program oxide 2−3 nm in thickness was grown and amorphous silicon (a:Si) was deposited conformally. The devices were completed by forming a control oxide layer (7−12 nm thick) on top of the nanocrystal array, then depositing the polysilicon gate (Figure 47). The devices exhibit low-voltage memory operation with promising retention and endurance properties.

4.4. Field Effect Transistors (FET)

An application of block copolymer patterning to the fabrication of a silicon field effect transistor (FET) has been demonstrated by Black.[160] In his approach, cylindrical microdomains are aligned within a topographic guiding pattern and serve as an etch mask for forming multiple nanowires of silicon. Figure 48 shows the stepwise fabrication steps for this FET. First, optical lithography and plasma etching were used to delineate a 200 nm wide and 25 nm deep trench in the 40 nm thick top silicon layer of a p-type silicon-on-insulator (SOI) wafer. The lithographic trench controls the alignment of cylindrical domains; in this instance, a six-nanowire array can be formed in the trench. A second level of optical lithography defined the device source/drain contacts. Titanium metal masks the source/drain regions during subsequent nanowire etching. The multi-nanowire FETs were completed with a 650 °C anneal to form Ti−Si_2 source/drain contacts.

4.5. Contact Holes

Contact holes or "vias" are notably difficult to fashion at small dimensions by conventional lithography, and it is not

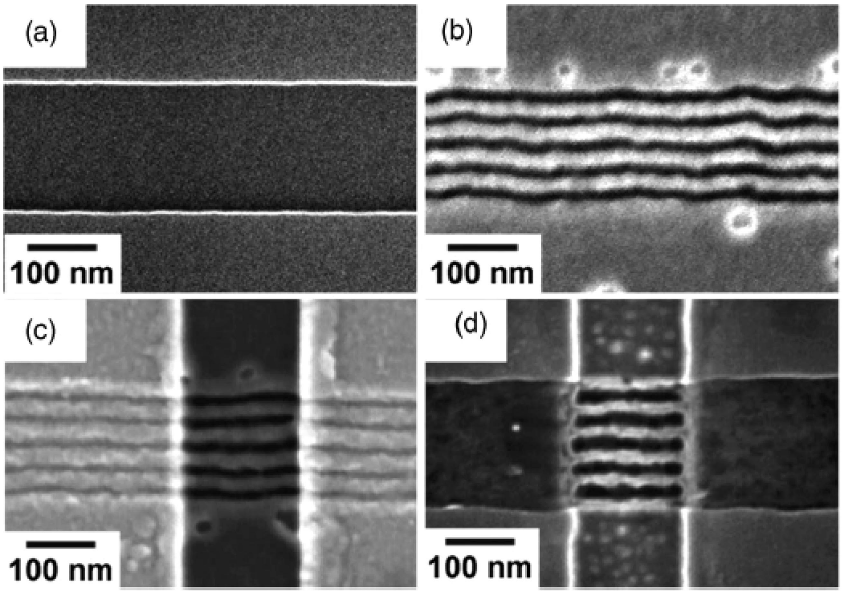

Figure 48. Nanowire array FET fabrication. (a) Lithographic definition of FET channel in a thin SOI layer. (b) Self-aligned polymer self-assembly subdivides lithographic feature. (c) Aligned lithographic definition of device source/drain regions. (d) Completed nanowire array FET (6 wire channel). (Reprinted with permission from ref 160. Copyright 2005 American Institute of Physics.)

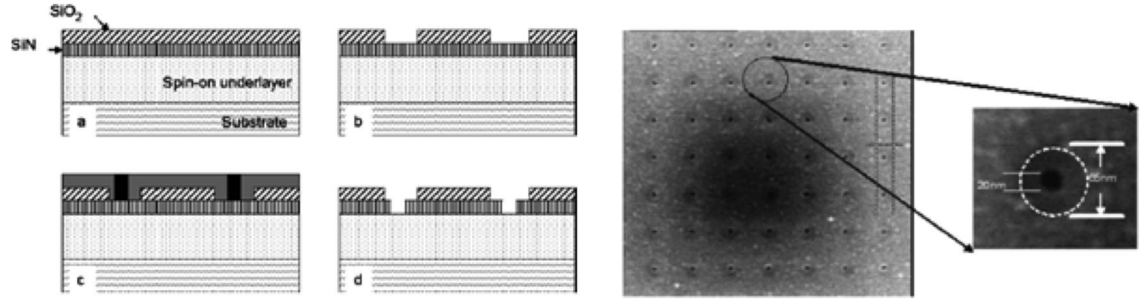

Figure 49. (Left) Process scheme of self-aligned PS-*b*-PMMA diblock copolymer. (a) Dual hard mask depositions (SiN/SiO_2). (b) SiO_2 hard mask open. (c) Application of diblock-copolymer film and annealing. (d) Pattern transfer into SiN hard mask with diblock copolymer followed by removal of polymer. Black represents PMMA, and light gray represents PS. (Right) Top-down SEM image of a uniform cylindrical block copolymer on large area. (Reprinted with permission from ref 162. Copyright 2007 American Vacuum Society.)

surprising that attempts have been made to use cylindrical microdomains in BCP films as an alternate route to forming such structures. Chang and Wong described the use of PS-*b*-PMMA thin films to define pores 20 nm in diameter as contact hole patterns for complementary metal oxide semiconductor (CMOS) device fabrication.[161] A similar approach was reported by Li and Yang, who formed sub-20 nm pores of PS-*b*-PMMA for creating contact holes on a full 300 mm silicon wafer.[162] Their process sequence is shown schematically in Figure 49. Two layers of hard mask materials, silicon nitride (SiN) and silicon oxide (SiO_2), were used in this approach. First, patterns of vias and lines were generated using conventional 193 nm photolithography and transferred into a silicon oxide hard mask using RIE. An asymmetric PS-*b*-PMMA with PMMA cylindrical domains was then deposited and annealed at 180 °C. After removing the PMMA domains using UV exposure and wet development, the cylindrical contact patterns were transferred to the SiN hard mask by plasma etching. The final contact hole pattern formed over a large area is shown in Figure 49 (right), which shows holes 20 nm in diameter within silicon oxide guide holes 65 nm in diameter.

5. Limitations

Polymer self-assembly affords a means to create immense numbers of nanoscale features in a simple, rapid, and inexpensive process where the spatial scale ultimately is controlled by chemical synthesis of macromolecules rather than by complex and costly tooling. These benefits come at some cost, however. Compared to the versatility and flexibility of modern-day lithographic technology, there are significant restrictions on how polymer self-assembly can be practically applied. We summarize those limitations here.

5.1. Device Design

Traditionally, a designer of integrated circuits could freely position individual device elements and interconnecting wiring to optimize circuit performance. When block copolymer patterning is evaluated for such applications, the regular nature and intrinsic periodicity of the microdomain patterns must be considered. Some structures, for example, a cross-point memory array[163] or a multigate FET device,[164] contain regular repeating features, and for these the use of block copolymer self-assembly can be readily envisioned. Other

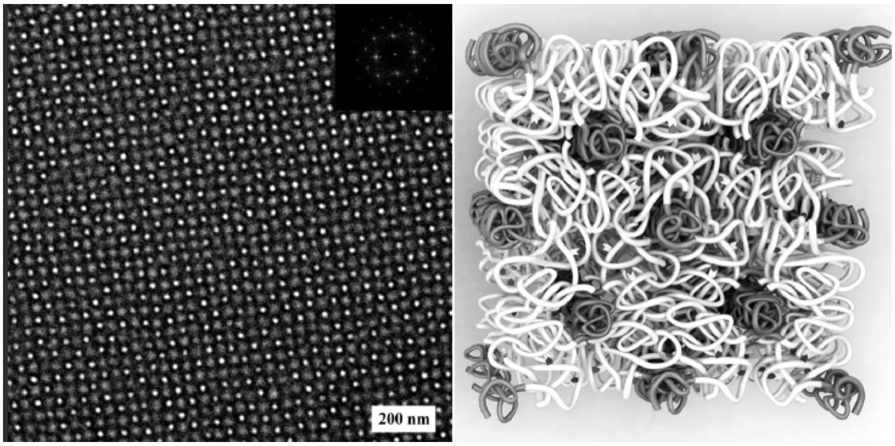

Figure 50. (Left) TEM image and associated Fourier transform (inset) of a solvent-annealed blend film of supramolecular block copolymers. (Right) Cartoon illustrating the proposed chain packing. (Reprinted with permission from ref 172. Copyright 2008 American Association for the Advancement of Science.)

designs, in particular those for logic circuits, pose more difficulty as there is less regularity in the device layout. However, there is currently a trend underway that plays to the strengths of polymer self-assembly. As optical lithographic technology evolves, restrictive design rules are established to circumvent the undesirable effects of optical diffraction that are magnified as target dimensions become much smaller than the exposing wavelength. Highly regular lithography-optimized layouts are being examined as a means to both maximize resolution and simplify the arduous design process.[165] The potential applicability of polymer self-assembly will expand if such regularized layouts grow commonplace. A methodology for incorporating DSA into device fabrication by parsing its layout into several masks has been described.[166]

5.2. Placement Control

In general, block-copolymer DSA requires careful tailoring of surface topographies and energies, usually in a spatially localized way, to produce the final pattern with suitable alignment and registration. The addition of steps to modify surface properties and protect the modified surfaces against damage during processing increases process complexity. This aspect will benefit from the development of specialized ancillary materials such as broadly compatible neutralization layers and imaging materials that allow direct formation of topographic guiding patterns and/or modification of surface properties.

There are pros and cons for topographic guiding patterns and chemical guiding patterns. As the typical dimensions of a topographic guiding structure are much larger than that of microdomains, it can be created easily by conventional lithography, but it must border the region where microdomains are to be formed and in so doing occupies a portion of the device real estate during the patterning step. This can be a drawback for many design layouts. Further, any imperfections or roughness in the topographic pattern are replicated in the block copolymer pattern, so the final pattern quality is limited by that of the guiding pattern.[131] In contrast, with the chemical pattern approach the guiding pattern is overlaid by the block copolymer pattern as it is formed, so no additional surface area must be allocated for it, and image rectification can lead to an overall improvement in final pattern quality.[149] One drawback of chemical patterning is that some portion the guiding pattern must have a dimension on the order of one-half the natural period L_0. While there are methods for forming isolated structures at that scale using conventional optical lithography, for example, by using a postlithography etch step to narrow a photoresist line, the additional processing adds complexity and cost.

5.3. Pattern Types

Only two major pattern types are commonly available from diblock copolymer thin films: hexagonally packed dots (from cylindrical or spherical domains) or periodic line patterns (from lamellar or cylindrical domains). However, current research using materials other than simple diblock copolymers is making a wider range of patterns available and will open opportunities for fabricating new device structures. Exotic patterns from triblock copolymers as shown in Figure 2 might be useful for generating nanostructures of novel functional devices. Indeed, many research groups have been exploring nanoscopic surface patterns from ABC triblock copolymers,[167−169] and patterns from still higher order block copolymers (e.g., multiblock copolymers) may find future applications. A recent report of Tang and co-workers on the generation of square patterns provides another example.[170−172] They used an approach combining supramolecular assembly of hydrogen-bonding units with controlled phase separation of diblock copolymers. As shown by the TEM image and the conceptual illustration in Figure 50, they fabricated highly ordered square arrays of sub-20 nm features using poly(ethylene oxide)-*b*-poly(styrene-*r*-4-hydroxystyrene) [PEO-*b*-P(S-*r*-4HS)] and poly(styrene-*r*-4-vinylpyridine)-*b*-poly(methyl methacrylate) [P(S-*r*-4VP)-*b*-PMMA] mixtures. This pattern type is directly compatible with the industry standard rectilinear coordinate system commonly used for device layout.

6. Functional Attributes

To guide research and development, the semiconductor industry has compiled a roadmap that specifies the functional requirements that any patterning technology must satisfy for future use.[173] These requirements provide a framework to evaluate the readiness of block copolymer patterning for practical application. In general, patterning by block copolymer self-assembly does not yet simultaneously meet all required specifications.

6.1. Defects

For future device generations, industry guidelines specify a number density for defects of 0.01 defects per square centimeter.[174] Early practical demonstrations of DSA displayed relatively large defect counts, and some more recent studies have addressed strategies for defect reduction. The sparse patterning approaches described earlier exhibit significantly lower defect levels; Ruiz et al., in their work studying sparse DSA for data storage applications, measured a defect level of less than 1 part in 10^4.[147] While defect levels are influenced by several factors, a materials system with a longer correlation length (grain size) for microdomains is expected to develop fewer defects.

6.2. Pattern Quality

Industry specifications for pattern quality are prescribed for lithographic resist materials based on the expected impact that variations in line widths and edge acuity of the final transferred pattern will have on device performance. Line-width variation is measured for the smallest or “critical” dimension (CD) in a pattern. One common measure of edge acuity is line-width roughness or LWR, which quantifies statistical variations of a resist line from its intended shape.[174] The industry targets for both of these parameters scale with image size. As an example, for a pattern with 16 nm CD, that dimension must be controlled to 0.7 nm 3σ while LWR must be no more than 0.8 nm 3σ.[173] A block copolymer based pattern must meet these same requirements if it is to serve in place of a photoresist image. The average dimension of microdomains is dictated by the size of the polymer chains, but dimensional nonuniformities between domains are observed and equate to variations in the CD. Moreover, dimensional variation in a guiding prepattern can lead to distortion of the spatial period of the self-assembled pattern.[175] In lamellar patterns, random fluctuations in the width of the microdomain equate to LWR.

6.3. Dimensional Scaling

The most recent published edition of the industry roadmap projects future requirements out to the 11 nm device generations. PS-*b*-PMMA exhibits a lower scaling limit of approximately 14 nm half-pitch for lamellar microdomains;[26] material systems that enable scaling beyond that limit will be required. To shrink the scale, shorter block lengths must be used since microdomain size scales with molecular weight. This decreases the repulsive interaction between dissimilar blocks, and to compensate the material must provide a proportional increase in the value of χ to ensure sufficient thermodynamic driving force for microphase separation. Hybrid block copolymer systems[66−70] and blends of homopolymers with triblock polymers[176] have been shown to exhibit characteristic microdomain spacing well below 10 nm.

6.4. Plasma Etch Characteristics

The ultimate fate of the final self-assembled pattern is to serve as a template by which the pattern is replicated in the substrate. In practice, this most often is affected using an RIE process, and the final pattern must therefore be designed to resist degradation in a plasma environment. Moreover, in many instances the pattern of microdomains is “developed” into a three-dimensional relief image by selectively removing one of the domains by a plasma process. For semiconductor device fabrication, one practical route to provide high plasma etching contrast is to incorporate a silicon-containing block. For example, previous work with poly(styrene-*b*-ferrocenyldimethylsilane) (PS-*b*-PFS)[130−132] or poly(styrene-*b*-dimethylsiloxane) (PS-*b*-PDMS)[138] showed high plasma etching contrast between two blocks. In an oxygen plasma, the silicon is converted to one that is a robust barrier against further erosion. Past experience dictates that a silicon polymer containing at least 10−12 wt % of silicon will provide an adequate protective oxide barrier layer in an oxygen plasma.[177]

7. Outlook

It is useful to consider how block copolymer self-assembly might find large-scale use in practical applications that require nanoscale patterns or nanostructures. Since this review focuses on applications in electronics, we restrict our discussion to that field.

Modern semiconductor technology is dependent on a base of knowledge and experience that enables the routine generation of patterns of arbitrary shape and complexity in a wide range of materials. That existing knowledge base and the economic investment it represents makes it unlikely that a completely new and disruptive patterning technology will suddenly displace existing practice. Instead, history shows that progress in the semiconductor field follows from the introduction of innovative technologies via incremental, evolutionary pathways. Some specialized device applications (for example, the formation of field emitter tips for information displays[178] or the air-gap structure described earlier in this review) make only modest demands for alignment, registration, and dimensional control and are well suited to be early adopters of block copolymer self-assembly. The recent progress cited in this review leads us to anticipate that block copolymers ultimately will be found in applications with more stringent requirements, applying directed self-assembly in concert with current patterning technologies to extend their dimensional scale. There remain technical issues that must be resolved, but given the uncertainty of how soon future lithographic alternatives will mature, there is now an opportunity for impact.

8. Abbreviations

χ	Flory−Huggins interaction parameter
N	number of monomers, degree of polymerization
PS-*b*-PI	poly(styrene-*b*-isoprene)
f	volume fraction
L_0	natural period of block-copolymer domain
SSL	strong segregation limit
WSL	weak segregation limit
IRS	intermediate segregation region
PS-*b*-PMMA	poly(styrene-*b*-methyl methacrylate)
AFM	atomic force microscopy
SAXS	small-angle X-ray scattering
TEM	transmission electron microscopy
PS-*b*-PB-*b*-PMMA	poly(styrene-*b*-butadiene-*b*-methyl methacrylate)
PS-*b*-PEB-*b*-PMMA, SEBM	poly(styrene-*b*-(ethylene-*co*-butylene)-*b*-methyl methacrylate)
PB	polybutadiene
PEB, EB	poly(ethylene-*co*-butylene)
P2VP	poly(2-vinylpyridine)
PI	polyisoprene
PS	polystyrene

PS-*b*-P4VP	poly(styrene-*b*-4-vinylpyridine)
P4VP	poly(4-vinylpyridine)
NDP	nonadecylphenol
MSA	methanesulfonic acid
PDP	pentadecylphenol
PI-*b*-PEO	poly(isoprene-*b*-ethylene oxide)
GLYMO	3-(glycidyloxypopyl)trimethoxysilane
Al(O-*s*-Bu)$_3$	aluminum *sec*-butoxide
PEO	poly(ethylene oxide)
PS-*b*-PEO	poly(styrene-*b*-ethylene oxide)
OS, PMS	organosilicate
SIMS	secondary ion mass spectroscopy
NR	neutron reflectivity
PS-*b*-P2VP	poly(styrene-*b*-2-vinylpyridine)
XPS	X-ray photoelectron spectroscopy
PS-*b*-PHOST	poly(styrene-*b*-hydroxystyrene)
PS-*b*-PnBMA	poly(styrene-*b*-*n*-butyl methacrylate)
SCF	self-consistent field
V	molar volume
r	gas constant
T	temperature
δ	solubility parameter
CS$_2$	carbon disulfide
THF	tetrahydrofuran
γ	interfacial energy
SANS	small angle neutron scattering
PFS-*b*-PLA	poly(4-fluorostyrene-*b*-D,L-lactide)
SEM	scanning electron microsocpy
ITO	indium tin oxide
q	wavenumber
iR	amplitude
DSA	directed self-assembly
PS-*b*-PFS	poly(styrene-*b*-ferrocenyldimethylsilane)
PS-*b*-PDMS	poly(styrene-*b*-dimethylsioxane)
RIE	reactive ion etching
PS-*b*-PEP	poly[styrene-*b*-(ethylene-*alt*-propylene)]
s	degree of commensurability
PDMS	polydimethylsiloxane
SEBS	poly(styrene-*b*-ethylene butylene-*b*-styrene)
PS-*b*-PB	poly(styrene-*b*-butadiene)
RC	resistance × capacitance
MOS	metal-oxide semiconductor
FET	field effect transistor
SOI	silicon-on-insulator
CMOS	complementary metal oxide semiconductor
SiN	silicon nitride
SiO$_2$	silicon oxide
PEO-*b*-P(S-*r*-4HS)	poly[(ethylene oxide)-*b*-(styrene-*r*-4-hydroxystyrene)]
P(S-*r*-4VP)-*b*-PMMA	poly[(styrene-*r*-4-vinylpyridine)-*b*-(methyl methacrylate)]
CD	critical dimension
LWR	line width roughness

9. References

(1) Park, C.; Yoon, J.; Thomas, E. L. *Polymer* **2003**, *44*, 6725.
(2) Krausch, G.; Magerle, R. *Adv. Mater.* **2002**, *14*, 1579.
(3) Hamley, I. W. *Angew. Chem., Int. Ed.* **2003**, *42*, 1692.
(4) Lazzari, M.; Lopez-Quintela, M. A. *Adv. Mater.* **2003**, *15*, 1583.
(5) Lu, W.; Sastry, A. M. *IEEE Trans. Semicond. Manuf.* **2007**, *20*, 421.
(6) Hawker, C. J.; Russell, T. P. *MRS Bull.* **2005**, *30*, 952.
(7) Li, M. Q.; Coenjarts, C. A.; Ober, C. K. *Adv. Polym. Sci.* **2005**, *190*, 183.
(8) Segalman, R. A. *Mater. Sci. Eng. R: Rep.* **2005**, *48*, 191.
(9) Cheng, J. Y.; Ross, C. A.; Smith, H. I.; Thomas, E. L. *Adv. Mater.* **2006**, *18*, 2505.
(10) Stoykovich, M. P.; Nealey, P. F. *Mater. Today* **2006**, *9*, 20.
(11) Krishnamoorthy, S.; Hinderling, C.; Heinzelmann, H. *Mater. Today* **2006**, *9*, 40.
(12) Li, M. Q.; Ober, C. K. *Mater. Today* **2006**, *9*, 30.
(13) Fasolka, M. J.; Mayes, A. M. *Annu. Rev. Mater. Res.* **2001**, *31*, 323.
(14) Darling, S. B. *Prog. Polym. Sci.* **2007**, *32*, 1152.
(15) Kim, H.-C.; Hinsberg, W. D. *J. Vac. Sci. Technol., A* **2008**, *26*, 1369.
(16) Bates, F. S.; Fredrickson, G. H. *Phys. Today* **1999**, *52*, 32.
(17) Abetz, V.; Simon, P. F. W. *Adv. Polym. Sci.* **2005**, *189*, 125.
(18) van Zoelen, W.; ten Brinke, G. *Soft Matter* **2009**, *5*, 1568.
(19) Bruning, J. H. *Proc. Soc. Photo-Opt. Eng.* **2007**, *6520*, 6520041.
(20) Mack, C. A. *Future Fab Int.* **2007**, *23*, 65.
(21) Schift, H. *J. Vac. Sci. Technol., B* **2008**, *26*, 458.
(22) Wua, B. Q.; Kumar, A. *J. Vac. Sci. Technol., B* **2007**, *25*, 1743.
(23) Park, M.; Harrison, C.; Chaikin, P. M.; Register, R. A.; Adamson, D. H. *Science* **1997**, *276*, 1401.
(24) Feldheim, D. L.; Keating, C. D. *Chem. Soc. Rev.* **1998**, *27*, 1.
(25) Wallraff, G. M.; Hinsberg, W. D. *Chem. Rev.* **1999**, *99*, 1801.
(26) Black, C. T.; Ruiz, R.; Breyta, G.; Cheng, J. Y.; Colburn, M. E.; Guarini, K. W.; Kim, H.-C.; Zhang, Y. *IBM J. Res. Dev.* **2007**, *51*, 605.
(27) Hamley, I. W. *The Physics of Block Copolymers*; Oxford University Press: Oxford, 1998.
(28) Leibler, L. *Macromolecules* **1980**, *13*, 1602.
(29) Smenov, A. N. *Macromolecules* **1986**, *25*, 4967.
(30) Ohta, T.; Kawasaki, K. *Macromolecules* **1986**, *19*, 2621.
(31) Helfand, E. *Macromolecules* **1975**, *8*, 552.
(32) Hashimoto, T.; Shibayama, M.; Kawai, H. *Macromolecules* **1980**, *13*, 1237.
(33) Bates, F. S.; Fredrickson, G. H. *Annu. Rev. Phys. Chem.* **1990**, *41*, 525.
(34) Fried, J. *Polymer Science and Technology*, 2nd ed.; Prentice Hall: Upper Saddle River, NJ, 2003.
(35) Flory, P. J. *Principles of Polymer Chemistry*; Cornell University Press: Ithaca, NY, 1953.
(36) Sivaniah, E.; Matsubara, S.; Zhao, Y.; Hashimoto, T.; Fukunaga, K.; Kramer, E. J.; Mates, T. E. *Macromolecules* **2008**, *41*, 2584.
(37) Matsushita, E.; Mori, K.; Saguchi, R.; Nakao, Y.; Noda, I.; Nagasawa, M. *Macromolecules* **1990**, *23*, 4313.
(38) Coulon, G.; Russell, T. P.; Deline, V. R.; Green, P. F. *Macromolecules* **1989**, *22*, 2581.
(39) Rebei, A.; De Pablo, J. *Phys. Rev. E* **2001**, 63.
(40) Melenkeviz, J.; Muthukumar, M. *Macromolecules* **1991**, *24*, 4199.
(41) Whitemore, M. D.; Noolandi, J. *J. Chem. Phys.* **1990**, *93*, 2946.
(42) Zheng, W.; Wang, Z.-G. *Macromolecules* **1995**, *28*, 7215.
(43) Auschra, C.; Stadler, R. *Macromolecules* **1993**, *26*, 2171.
(44) Stadler, R.; Auschra, C.; Beckmann, J.; Krappe, U.; Voigt-Martin, I.; Leibler, L. *Macromolecules* **1995**, *28*, 3080.
(45) Krappe, U.; Stadler, R.; Voigt-Martin, I. *Macromolecules* **1995**, *28*, 4558.
(46) Breiner, U.; Krappe, U.; Abetz, V.; Stadler, R. *Macromol. Chem. Phys.* **1997**, *198*, 1051.
(47) Breiner, U.; Krappe, U.; Stadler, R. *Macromol. Rapid Commun.* **1996**, *17*, 567.
(48) Matsushita, Y.; Mogi, Y.; Mukai, H.; Watanabe, J.; Noda, I. *Polymer* **1994**, *35*, 246.
(49) Hermel, T. J.; Hahn, S. F.; Chaffin, K. A.; Gerberich, W. W.; Bates, F. S. *Macromolecules* **2003**, *36*, 2190.
(50) Wu, L. F.; Lodge, T. P.; Bates, F. S. *Macromolecules* **2004**, *37*, 8184.
(51) Nagata, Y.; Masuda, J.; Noro, A.; Cho, D. Y.; Takano, A.; Matsushita, Y. *Macromolecules* **2005**, *38*, 10220.
(52) Subbotin, A.; Klymko, T.; ten Brinke, G. *Macromolecules* **2007**, *40*, 2915.
(53) Masuda, J.; Takano, A.; Nagata, Y.; Noro, A.; Matsushita, Y. *Phys. Rev. Lett.* **2006**, *97*, 098301.
(54) Masuda, J.; Takano, A.; Suzuki, J.; Nagata, Y.; Noro, A.; Hayashida, K.; Matsushita, Y. *Macromolecules* **2007**, *40*, 4023027.
(55) Ruokolainen, J.; ten Brinke, G.; Ikkala, O. *Adv. Mater.* **1999**, *11*, 777.
(56) Ruokolainen, J.; Makinen, R.; Torkkeli, M.; Makela, T.; Serimaa, R.; ten Brinke, G.; Ikkala, O. *Science* **1998**, *280*, 557.
(57) Maki-Ontto, R.; de Moel, K.; de Odorico, W.; Ruokolainen, J.; Stamm, M.; ten Brinke, G.; Ikkala, O. *Adv. Mater.* **2001**, *13*, 117.
(58) Tiitu, M.; Volk, N.; Torkkeli, M.; Serimaa, R.; ten Brinke, G.; Ikkala, O. *Macromolecules* **2004**, *37*, 7364.
(59) Valkama, S.; Kosonen, H.; Ruokolainen, J.; Haatainen, T.; Torkkeli, M.; Serimaa, R.; Ten Brinke, G.; Ikkala, O. *Nat. Mater.* **2004**, *3*, 872.
(60) Kresge, C. T.; Leonowicz, M. E.; Roth, W. J.; Vartuli, J. C.; Beck, J. S. *Nature* **1992**, *359*, 710.
(61) Templin, M.; Franck, A.; DuChesne, A.; Leist, H.; Zhang, Y. M.; Ulrich, R.; Schadler, V.; Wiesner, U. *Science* **1997**, *278*, 1795.
(62) Simon, P. F. W.; Ulrich, R.; Spiess, H. W.; Wiesner, U. *Chem. Mater.* **2001**, *13*, 3464.
(63) Huo, Q.; Leon, R.; Petroff, P. M.; Stucky, G. D. *Science* **1995**, *268*, 1324.
(64) Pai, R. A.; Humayun, R.; Schulberg, M. T.; Sengupta, A.; Sun, J. N.; Watkins, J. J. *Science* **2004**, *303*, 507.

(65) Lu, Y. F.; Ganguli, R.; Drewien, C. A.; Anderson, M. T.; Brinker, C. J.; Gong, W. L.; Guo, Y. X.; Soyez, H.; Dunn, B.; Huang, M. H.; Zink, J. I. *Nature* **1997**, *389*, 364.

(66) Freer, E. M.; Krupp, L. E.; Hinsberg, W. D.; Rice, P. M.; Hedrick, J. L.; Cha, J. N.; Miller, R. D.; Kim, H.-C. *Nano Lett.* **2005**, *5*, 2014.

(67) Sundström, L.; Krupp, L.; Delenia, E.; Rettner, C.; Sanchez, M.; Hart, M. W.; Kim, H.-C.; Zhang, Y. *Appl. Phys. Lett.* **2006**, *88*, 243107.

(68) Cheng, J. Y.; Pitera, J.; Park, O. H.; Flickner, M.; Ruiz, R.; Black, C. T.; Kim, H.-C. *Appl. Phys. Lett.* **2007**, *91*, 143106.

(69) Park, S. M.; Park, O. H.; Cheng, J. Y.; Rettner, C. T.; Kim, H.-C. *Nanotechnology* **2008**, *19*, 455304.

(70) Kim, H.-C.; Rettner, C. T.; Sundstrom, L. *Nanotechnology* **2008**, *19*, 35301.

(71) Chuang, V. P.; Jung, W.; Ross, C. A.; Cheng, J. Y.; Park, O. H.; Kim, H.-C. *J. Appl. Phys.* **2008**, *103*, 074301.

(72) Jagannathan, H.; Deal, M.; Nishi, Y.; Kim, H.-C.; Freer, E. M.; Sundstrom, L.; Topuria, T.; Rice, P. M. *J. Vac. Sci. Technol. B* **2006**, *24*, 2220.

(73) Lopes, W. L.; Jaeger, H. M. *Nature* **2001**, *414*, 735.

(74) Sohn, B. H.; Seo, B. H. *Chem. Mater.* **2001**, *13*, 1752.

(75) Bockstaller, M. R.; Mickiewicz, R. A.; Thomas, E. L. *Adv. Mater.* **2005**, *17*, 1331.

(76) Kim, B. J.; Bang, J.; Hawker, C. J.; Kramer, E. J. *Macromolecules* **2006**, *39*, 4108.

(77) Park, S. C.; Kim, B. J.; Hawker, C. J.; Kramer, E. J.; Bang, J.; Ha, J. S. *Macromolecules* **2007**, *40*, 8119.

(78) Chai, J.; Wang, D.; Fan, X.; Buriak, J. M. *Nat. Nanotechnol.* **2007**, *2*, 500.

(79) Chai, J.; Buriak, J. M. *ACS Nano* **2008**, *2*, 489.

(80) Thompson, R. B.; Ginzburg, V. V.; Matsen, M. W.; Balazs, A. C. *Science* **2001**, *292*, 2469.

(81) Thompson, R. B.; Ginzburg, V. V.; Matsen, M. W.; Balazs, A. C. *Macromolecules* **2002**, *35*, 1060.

(82) Cheng, J. Y.; Ross, C. A. *Polymer Thin Films*; World Scientific: Hackensack, NJ, 2009; p 77.

(83) Kim, S.; Briber, R. M.; Karim, A.; Jones, R. L.; Kim, H. C. *Macromolecules* **2007**, *40*, 4102.

(84) Thurn-Albrecht, T.; Steiner, R.; DeRouchey, J.; Stafford, C. M.; Huang, E.; Bal, M.; Tuominen, M.; Hawker, C. J.; Russell, T. P. *Adv. Mater.* **2000**, *12*, 1138.

(85) Kim, H. C.; Jia, X. Q.; Stafford, C. M.; Kim, D. H.; McCarthy, T. J.; Tuominen, M.; Hawker, C. J.; Russell, T. P. *Adv. Mater.* **2001**, *13*, 795.

(86) Pederson, L. A. *J. Electrochem. Soc.* **1982**, *129*, 205.

(87) Ting, Y. H.; Park, S. M.; Liu, C. C.; Liu, X. S.; Himpsel, F. J.; Nealey, P. F.; Wendt, A. E. *J. Vac. Sci. Technol. B* **2008**, *26*, 1684.

(88) Russell, T. P.; Coulon, G.; Deline, V. R.; Miller, D. C. *Macromolecules* **1989**, *22*, 4600.

(89) Green, P. F.; Christensen, T. M.; Russell, T. P. *Macromolecules* **1991**, *24*, 252.

(90) Mayes, A. M.; Russell, T. P.; Bassereau, P.; Baker, S. M.; Smith, G. I. *Macromolecules* **1994**, *27*, 749.

(91) Cai, Z.-H.; Huang, K.; Montano, P. A.; Russell, T. P.; Bai, J. M.; Zajac, G. W. *J. Chem. Phys.* **1993**, *98*, 2367.

(92) Coulon, G.; Ausserre, D.; Russell, T. P. *J. Phys. (Paris)* **1990**, *51*, 777.

(93) Coulon, G.; Collin, B.; Ausserre, D.; Chatenay, D.; Russell, T. P. *J. Phys. (Paris)* **1990**, *51*, 2801.

(94) Anastasiadis, S. H.; Russell, T. P.; Satija, S. K.; Majkrzak, C. F. *J. Chem. Phys.* **1990**, *92*, 5677.

(95) Spatz, J. P.; Sheiko, S.; Möller, M. *Adv. Mater.* **1996**, *8*, 513.

(96) Spatz, J. P.; Möller, M.; Noeske, M.; Behm, R. J.; Pietralla, M. *Macromolecules* **1997**, *30*, 3874.

(97) Spatz, J. P.; Eibeck, P.; Mossmer, S.; Möller, M.; Herzog, T.; Ziemann, P. *Adv. Mater.* **1998**, *10*, 849.

(98) Potemkin, I. I.; Kramarenko, E. Y.; Khokhlov, A. R.; Winkler, R. G.; Reineker, P.; Eibeck, P.; Spatz, J. P.; Möller, M. *Langmuir* **1999**, *15*, 7290.

(99) Kramarenko, E. Y.; Potemkin, I. I.; Khokhlov, A. R.; Winkler, R. G.; Reineker, P. *Macromolecules* **1999**, *32*, 3495.

(100) Spatz, J. P.; Eibeck, P.; Mossmer, S.; Möller, M.; Kramarenko, E. Y.; Khalatur, P. G.; Potemkin, I. I.; Khokhlov, A. R.; Winkler, R. G.; Reineker, P. *Macromolecules* **2000**, *33*, 150.

(101) Potemkin, I. I.; Möller, M. *Macromolecules* **2005**, *38*, 2999.

(102) Yoon, B.; Huh, J.; Ito, H.; Frommer, J.; Sohn, B. H.; Kim, J. H.; Thomas, E. L.; Park, C.; Kim, H.-C. *Adv. Mater.* **2007**, *19*, 3342.

(103) Morkved, T. L.; Jaeger, H. M. *Europhys. Lett.* **1997**, *40*, 643.

(104) Morkved, T. L.; Lopes, W. A.; Hahm, J.; Sibener, S. J.; Jaeger, H. M. *Polymer* **1998**, *39*, 3871.

(105) Russell, T. P.; Menelle, A.; Anastasiadis, S. H.; Satija, S. K.; Majkrzak, C. F. *Macromolecules* **1991**, *24*, 6263.

(106) Fasolka, M. J.; Harris, D. J.; Mayes, A. M.; Yoon, M.; Mochrie, S. G. J. *Phys. Rev. Lett.* **1997**, *79*, 3018.

(107) Fasolka, M. J.; Banerjee, P.; Mayes, A. M.; Pickett, G.; Balazs, A. C. *Macromolecules* **2000**, *33*, 5702.

(108) Peng, J.; Kim, D. H.; Knoll, W.; Xuan, Y.; Li, B. Y.; Han, Y. C. *J. Chem. Phys.* **2006**, *125*, 064702.

(109) Peng, J.; Xuan, Y.; Wang, H. F.; Yang, Y. M.; Li, B. Y.; Han, Y. C. *J. Chem. Phys.* **2004**, *120*, 11163.

(110) Xuan, Y.; Peng, J.; Cui, L.; Wang, H. F.; Li, B. Y.; Han, Y. C. *Macromolecules* **2004**, *37*, 7301.

(111) Mansky, P.; Russell, T. P.; Hawker, C. J.; Mays, J.; Cook, D. C.; Satija, S. K. *Phys. Rev. Lett.* **1997**, *79*, 237.

(112) Mansky, P.; Liu, Y.; Huang, E.; Russell, T. P.; Hawker, C. J. *Science* **1997**, *275*, 1458.

(113) Mansky, P.; Russell, T. P.; Hawker, C. J.; Pitsikalis, M.; Mays, J. *Macromolecules* **1997**, *30*, 6810.

(114) Huang, E.; Russell, T. P.; Harrison, C.; Chaikin, P. M.; Register, R. A.; Hawker, C. J.; Mays, J. *Macromolecules* **1998**, *31*, 7641.

(115) Huang, E.; Pruzinsky, S.; Russell, T. P.; Mays, J.; Hawker, C. J. *Macromolecules* **1999**, *32*, 5299.

(116) Huang, E.; Mansky, P.; Russell, T. P.; Harrison, C.; Chaikin, P. M.; Register, R. A.; Hawker, C. J.; Mays, J. *Macromolecules* **2000**, *33*, 80.

(117) Thurn-Albrecht, T.; Schotter, J.; Kastle, C. A.; Emley, N.; Shibauchi, T.; Krusin-Elbaum, L.; Guarini, K.; Black, C. T.; Tuominen, M. T.; Russell, T. P. *Science* **2000**, *290*, 2126.

(118) Crossland, E. J. W.; Ludwigs, S.; Hillmyer, M. A.; Steiner, U. *Soft Matter* **2007**, *3*, 94.

(119) Yoshimoto, K.; Stoykovich, M. P.; Cao, H. B.; de Pablo, J. J.; Nealey, P. F.; Drugan, W. J. *J. Appl. Phys.* **2004**, *96*, 1857.

(120) Jeong, U.; Ryu, D. Y.; Kho, D. H.; Kim, J. K.; Goldbach, J. T.; Kim, D. H.; Russell, T. P. *Adv. Mater.* **2004**, *16*, 533.

(121) Sivaniah, E.; Hayashi, Y.; Iino, M.; Hashimoto, T.; Fukunaga, K. *Macromolecules* **2003**, *36*, 5894.

(122) Tsori, Y.; Andelman, D. *Macromolecules* **2003**, *36*, 8560.

(123) Tsori, Y.; Sivaniah, E.; Andelman, D.; Hashimoto, T. *Macromolecules* **2005**, *38*, 7193.

(124) Sivaniah, E.; Hayashi, Y.; Matsubara, S.; Kiyono, S.; Hashimoto, T.; Kukunaga, K.; Kramer, E. J.; Mates, T. *Macromolecules* **2005**, *38*, 1837.

(125) Seeger, D. E.; LaTulipe, D. C.; Kunz, R. R.; Garza, C. M.; Hanratty, M. A. *IBM J. Res. Dev.* **1997**, *41*, 105.

(126) Park, O. H.; Cheng, J. Y.; Hart, M. W.; Topuria, T.; Rice, P. M.; Krupp, L. E.; Miller, R. D.; Ito, H.; Kim, H.-C. *Adv. Mater.* **2008**, *20*, 738.

(127) Lin, Z. Q.; Kim, D. H.; Wu, X. D.; Boosahda, L.; Stone, D.; LaRose, L.; Russell, T. P. *Adv. Mater.* **2002**, *14*, 1373.

(128) Kim, S. H.; Misner, M. J.; Xu, T.; Kimura, M.; Russell, T. P. *Adv. Mater.* **2004**, *16*, 226.

(129) Segalman, R. A.; Yokoyama, H.; Kramer, E. J. *Adv. Mater.* **2001**, *13*, 1152.

(130) Cheng, J. Y.; Ross, C. A.; Thomas, E. L.; Smith, H. I.; Vancso, G. J. *Appl. Phys. Lett.* **2002**, *81*, 3657.

(131) Cheng, J. Y.; Ross, C. A.; Thomas, E. L.; Smith, H. I.; Vancso, G. J. *Adv. Mater.* **2003**, *15*, 1599.

(132) Cheng, J. Y.; Mayes, A. M.; Ross, C. A. *Nat. Mater.* **2004**, *3*, 823.

(133) Sundrani, D.; Darling, S. B.; Sibener, S. J. *Nano Lett.* **2004**, *4*, 273.

(134) Sundrani, D.; Darling, S. B.; Sibener, S. J. *Langmuir* **2004**, *20*, 5091.

(135) Sundrani, D.; Sibener, S. J. *Macromolecules* **2002**, *35*, 8531.

(136) Park, S. M.; Stoykovich, M. P.; Ruiz, R.; Zhang, Y.; Black, C. T.; Nealey, P. E. *Adv. Mater.* **2007**, *19*, 607.

(137) Ruiz, R.; Ruiz, N.; Zhang, Y.; Sandstrom, R. L.; Black, C. T. *Adv. Mater.* **2007**, *19*, 2157.

(138) Bita, I.; Yang, J. K. W.; Jung, Y. S.; Ross, C. A.; Thomas, E. L.; Berggren, K. K. *Science* **2008**, *321*, 939.

(139) Yamaguchi, T.; Yamaguchi, H. *J. Photopolym. Sci. Technol.* **2006**, *19*, 385.

(140) Yamaguchi, Y.; Yamaguchi, H. *Polym. Mater.: Sci. Eng.* **2006**, *51*, 247.

(141) Ruiz, R.; Ruiz, N.; Zhang, Y.; Sandstrom, R. L.; Black, C. T. *Adv. Mater.* **2007**, *19*, 2157.

(142) Park, S. M.; Berry, B. C.; Dobisz, E.; Kim, H.-C. *Soft Matter* **2009**, *5*, 957.

(143) Park, S.; Lee, D. H.; Xu, J.; Kim, B.; Hong, S. W.; Jeong, U.; Xu, T.; Russell, T. P. *Science* **2009**, *323*, 1030.

(144) Rockford, L.; Liu, Y.; Mansky, P.; Russell, T. P.; Yoon, M.; Mochrie, S. G. J. *Phys. Rev. Lett.* **1999**, *82*, 2602.

(145) Kim, S. O.; Solak, H. H.; Stoykovich, M. P.; Ferrier, N. J.; de Pablo, J. J.; Nealey, P. F. *Nature* **2003**, *424*, 411.

(146) Stoykovich, M. P.; Muller, M.; Kim, S. O.; Solak, H. H.; Edwards, E. W.; de Pablo, J. J.; Nealey, P. F. *Science* **2005**, *308*, 1442.

(147) Ruiz, R.; Kang, H. M.; Detcheverry, F. A.; Dobisz, E.; Kercher, D. S.; Albrecht, T. R.; de Pablo, J. J.; Nealey, P. F. *Science* **2008**, *321*, 936.

(148) Tada, Y.; Akasaka, S.; Yoshida, H.; Hasegawa, H.; Dobisz, E.; Kercher, D.; Takenaka, M. *Macromolecules* **2008**, *41*, 9267.
(149) Cheng, J. Y.; Rettner, C. T.; Sanders, D. P.; Kim, H.-C.; Hinsberg, W. D. *Adv. Mater.* **2008**, *20*, 3155.
(150) Li, L.; Yokoyama, H. *Adv. Mater.* **2005**, *17*, 1432.
(151) Li, H. W.; Huck, W. T. S. *Nano Lett.* **2004**, *4*, 1633.
(152) Mansky, P.; Chaikin, P. M. *J. Mater. Sci.* **1995**, *30*, 1987.
(153) Park, M.; Chaikin, P. M.; Register, R. A.; Adamson, D. H. *Appl. Phys. Lett.* **2001**, *79*, 257.
(154) Cheng, J. Y.; Ross, C. A.; Chan, V. Z. H.; Thomas, E. L.; Lammertink, R. G. H.; Vancso, G. J. *Adv. Mater.* **2001**, *13*, 1174.
(155) Lee, W. W.; Ho, P. S. *MRS Bull.* **1997**, *22*, 19.
(156) Ponoth, S.; Horak, D.; Colburn, M. E.; Breyta, G.; Huang, E.; Sucharitaves, J.; Landis, H.; Lisi, A.; Liu, X. S.; Vo, T.; Johnson, R.; Li, W.; Purushothaman, S.; Cohen, S.; Hu, C.-K.; Kim, H.-C.; Clevenger, L.; Fuller, N.; Nogami, T.; Spooner, T.; Edelstein, D. The Electrochemical Society, conference proceedings, Fall 2008.
(157) Black, C. T.; Guarini, K. W.; Milkove, K. R.; Baker, S. M.; Russell, T. P.; Tuominen, M. T. *Appl. Phys. Lett.* **2001**, *79*, 409.
(158) Black, C. T.; Guarini, K. W.; Zhang, Y.; Kim, H. J.; Benedict, J.; Sikorski, E.; Babich, I. V.; Milkove, K. R. *IEEE Electron Device Lett.* **2004**, *25*, 622.
(159) Guarini, K. W.; Black, C. T.; Zhang, Y.; Babich, I. V.; Sikorski, E. M.; Gignac, L. M. *IEEE Int. Electron Device Meeting* **2003**, 541.
(160) Black, C. T. *Appl. Phys. Lett.* **2005**, *87*, 163116.
(161) Chang, L.-W.; Wong, H.-S. P. *Proc. SPIE* **2006**, *6156*, 615611.
(162) Li, W. K.; Yang, S. *J. Vac. Sci. Technol. B* **2007**, *25*, 1982.
(163) Burr, G. W.; Kurdi, B. N.; Scott, J. C.; Lam, C. H.; Gopalakrishnan, K.; Shenoy, R. S. *IBM J. Res. Dev.* **2008**, *52*, 449.
(164) Schmitt-Landsiedel, D.; Werner, C. *Solid-State Electron.* **2009**, *53*, 411.
(165) Calhoun, B. H.; Cao, Y.; Li, X.; Mai, K.; Pileggi, L. T.; Rutenbar, R. A.; Shepard, K. L. *Proc. IEEE* **2008**, *96*, 343.
(166) Schellenberg, F. M.; Torres, J. A. R. *Proc. Soc. Photo-Opt. Eng.* **2006**, *6151*, 61513L1.
(167) Boker, A.; Muller, A. H. E.; Krausch, G. *Macromolecules* **2001**, *34*, 7477.
(168) Elbs, H.; Drummer, C.; Abetz, Volker.; Krausch, G. *Macromolecules* **2002**, *35*, 5570.
(169) Boschetti-de-Fierro, A.; Spindler, L.; Reiter, G.; Olmos, D.; Magonov, S.; Abetz, V. *Macromolecules* **2007**, *40*, 5487.
(170) Bang, J.; Kim, S. H.; Drockenmuller, E.; Misner, M. J.; Russell, T. P.; Hawker, C. J. *J. Am. Chem. Soc.* **2006**, *128*, 7622.
(171) Tang, C. B.; Bang, J.; Stein, G. E.; Fredrickson, G. H.; Hawker, C. J.; Kramer, E. J.; Sprung, M.; Wang, J. *Macromolecules* **2008**, *41*, 4328.
(172) Tang, C. B.; Lennon, E. M.; Fredrickson, G. H.; Kramer, E. J.; Hawker, C. J. *Science* **2008**, *322*, 429.
(173) *International Technology Roadmap for Semiconductors (ITRS) 2007 Edition*; Semiconductor Industry Association: San Jose, CA, 2007.
(174) Gogolides, E.; Constantoudis, V.; Patsis, G. P.; Tserepi, A. *Microelectron. Eng.* **2006**, *83*, 1067.
(175) Edwards, E. W.; Muller, M.; Stoykovich, M. P.; Solak, H. H.; de Pablo, J. J.; Nealey, P. F. *Macromolecules* **2007**, *40*, 90.
(176) Tirumala, V. R.; Daga, V.; Bosse, A. W.; Romang, A.; Ilavsky, J.; Lin, E. K.; Watkins, J. J. *Macromolecules* **2008**, *41*, 7978.
(177) Miller, R. D.; Wallraff, G. M. *Adv. Mater. Opt. Electron.* **1994**, *4*, 95.
(178) Weigl, F.; Fricker, S.; Boyen, H. G.; Dietrich, C.; Koslowski, B.; Plettl, A.; Pursche, O.; Ziemann, P.; Walther, P.; Hartmann, C.; Ott, M.; Moller, M. *Diamond Relat. Mater.* **2006**, *15*, 1689.

CR900159V